Multi-scale Analysis of Surface Heterogeneity Induced Convection on Isentropic Coordinates

Jingyi Chen,[a] Samson Hagos,[a] Heng Xiao,[a] Jerome Fast,[a] and Zhe Feng[a]

[a]*Pacific Northwest National Laboratory, Richland, WA, USA*

Corresponding author: Jingyi Chen, jingyi.chen@pnnl.gov

File generated with AMS Word template 1.0

Early Online Release: This preliminary version has been accepted for publication in *Journal of the Atmospheric Sciences*, may be fully cited, and has been assigned DOI 10.1175/JAS-D-21-0198.1. The final typeset copyedited article will replace the EOR at the above DOI when it is published.

ABSTRACT

This study uses semi-idealized simulations to investigate multi-scale processes induced by the heterogeneity of soil moisture observed during the 2016 Holistic Interactions of Shallow Clouds, Aerosols, and Land-Ecosystems (HI-SCALE) field campaign. The semi-idealized simulations have realistic land heterogeneity, but large-scale winds are removed. Analysis on isentropic coordinates enables the tracking of circulation that transports energy vertically and facilitates the identification of the primary convective processes induced by realistic land heterogeneity. The isentropes associated with upward motion are found to connect the ground characterized by high latent heat flux to cloud bases directly over the ground with high sensible heat flux, while isentropes associated with downward motion connect precipitation to the ground characterized by high sensible heat fluxes. The mixing of dry, warm parcels ascending from the ground with high sensible heat fluxes and moist parcels from high latent heat regions leads to cloud formation. This new mechanism explains how soil moisture heterogeneity provides the key ingredients such as buoyancy and moisture for shallow cloud formation. We also found that the sub-mesoscale dominates upward energy transport in the boundary layer, while mesoscale circulations contribute to vertical energy transport above the boundary layer. Our novel method better illustrates and elucidates the nature of land atmospheric interactions under irregular and realistic soil moisture patterns.

Accepted for publication in *Journal of the Atmospheric Sciences*. DOI 10.1175/JAS-D-21-0198.1.

SIGNIFICANCE STATEMENT

Models that resolve boundary layer turbulence and clouds have been used extensively to understand processes controlling land-atmosphere interactions, but many of their configurations and computational expense limit the use of variable land properties. This study aims to understand how heterogeneous land properties over multiple spatial scales affect energy redistribution by moist convection. Using a more realistic land representation and isentropic analyses, we found that high sensible heat flux regions are associated with relatively higher vertical velocity near the surface, and the high latent heat flux regions are associated with relatively higher moist energy. The mixing of parcels rising from these two regions results in the formation of shallow clouds.

Accepted for publication in *Journal of the Atmospheric Sciences*. DOI 10.1175/JAS-D-21-0198.1.

1. Introduction

Moist convection redistributes the energy from the surface to high altitudes [*Stevens*, 2005]. Over midlatitude continental areas, such as the Southern Great Plains (SGP) in the United States, daytime moist convection is often observed with initiation in the morning. Cold pools-induced mesoscale circulations contribute to the afternoon convection events during the summer [*Dai et al.*, 1999; *Nesbitt and Zipser*, 2003; *Randall et al.*, 1991; *Wallace*, 1975; *Zhang and Klein*, 2010]. For those convective events, the turbulent ascent of warm, moist air is compensated by downdrafts of cold and dry air. In addition to boundary layer processes, the coupling between the land surface and atmosphere modifies the surface energy partitioning and hence the state of the overlying atmosphere and afternoon moist convective cells [*Gentine et al.*, 2013]. This study investigates the impacts of surface heterogeneity on the energy redistribution associated with shallow convection initiation in the morning and subsequent transition to deep convection in the afternoon.

Previous research showed that landscape heterogeneities induce secondary circulation, which contributes to the formation of planetary boundary layer characteristics and convective clouds [*Avissar and Liu*, 1996; *Avissar and Schmidt*, 1998; *Hadfield et al.*, 1991; *Huang and Margulis*, 2013; *Rieck et al.*, 2015; *Rochetin et al.*, 2017; *Taylor et al.*, 2007]. The picture of the convection over heterogeneous surfaces is mostly based on idealized land-surface property distributions (e.g., chessboard patterns). Previous studies showed that 1) the induced secondary circulation transports moisture from wet to dry patches near-surface [e.g., *Segal and Arritt*, 1992], 2) the stronger updrafts over the dry patches combining with the moisture transported from the neighboring wet patches make dry patches a prime spot for moist convection when ambient forcing is weak, [e.g., *Kang*, 2016; *Taylor et al.*, 2011], and 3) the subsidence over the wet patches tends to warm and dry PBL in those regions [e.g., *Lohou and Patton*, 2014].

Accepted for publication in *Journal of the Atmospheric Sciences*. DOI 10.1175/JAS-D-21-0198.1.

However, the mechanisms that induce local variations in convection for more realistic spatial distributions of surface properties are not well understood due to the lack of observational data and complex surface properties. For example, *Rochetin et al.* [2017] analyzed how the circulation induced by a surface sensible heat flux heterogeneity impacts deep convective initiation. They found that using a surface sensible heat flux map with realistic spatial heterogeneity triggers convection earlier in the day than a more idealized surface configuration. *Kang and Ryu* [2016] generated two-dimensional variations in land properties with prescribed spectral slope, which is more realistic than one-dimensional sinusoidal or chessboard patterns but still simpler than real variations in land properties. They found that the vertical transport of mesoscale moisture and heat fluctuations by turbulent updrafts play important roles in the transition from shallow clouds to deep clouds, which occurs when the imposed variations in surface heat flux are generally organized at the mesoscale. *Garcia-Carreras et al.* [2011] investigated the mechanisms in convective initiation over forest and cropland with constant surface flux and varied Bowen ratio (i.e., the ratio of surface sensible heat flux to the latent heat flux) only according to the land use type. They found a domain maximum equivalent potential temperature at the convergence zone, which favors convective events by locally increasing the buoyancy of lifted parcels.

Though most of these studies simulated convection initiation using idealized and semi-idealized surface variations, some studies suggested that realistic surface heterogeneity derived from observations leads to predictions of more accurate clouds [*Williams et al.*, 2020; *Wu et al.*, 2015]. *Fast et al.* [2019b] conducted Large Eddy Simulations (LES) coupled with an interactive land model to examine the impacts of soil property variations and small-scale vertical variations in the initial atmospheric state on the complex convective cloud population observed on a selected day during the Holistic Interactions of Shallow Clouds, Aerosols, and

Accepted for publication in *Journal of the Atmospheric Sciences*. DOI 10.1175/JAS-D-21-0198.1.

Land-Ecosystems (HI-SCALE) field campaign over the ARM SGP site [*Fast et al.*, 2019a]. They took advantage of ARM and Oklahoma Mesonets [*McPherson*, 2007] and the Global land Evaporation Amsterdam Model (GLEAM) to construct an observation-based soil moisture spatial distribution across Oklahoma and Kansas. Measurements evaluating those simulated clouds include ground-based and aircraft observations and Moderate Resolution Imaging Spectroradiometer (MODIS) satellite images of cloud distributions. Using a variety of sensitivity tests, they concluded that soil moisture variability is the primary factor in controlling cumulus formation early in the day. However, that study did not analyze energy transport and the circulation mechanisms associated with realistic surface heterogeneity.

To estimate the thermodynamic behavior of moist convection from Eulerian three-dimensional atmospheric variable fields, *Pauluis and Mrowiec* [2013] analyzed model predictions of convective overturning on isentropic coordinates. The three-dimensional mass flux is reduced to two dimensions by averaging variables on isentropic slices. Thus, air parcel trajectories are represented by the stream function, which is an integral of mass flux along the equivalent potential temperature axis (see more details in *Pauluis and Mrowiec* [2013]). *Chen et al.* [2018] investigated multi-scale atmospheric overturning during the Indian summer monsoon by adopting isentropic analysis to sort vertical mass fluxes. They decomposed the overturning into basin scale, synoptic-scale, and convective scale, and they found that convective-scale overturning dominates in the lower troposphere while regional scale overturning extends deeper in the troposphere. To quantify the thermodynamic transformations, *Pauluis* [2016] introduced the Mean Airflow as Lagrangian Dynamics Approximation (MAFALDA) method to extract the thermodynamical circulations with trajectories based on isentropic analysis. They estimated the impacts of climate change on convective thermodynamic cycles by the MAFALDA method, and found that the ratio of the

Accepted for publication in *Journal of the Atmospheric Sciences*. DOI 10.1175/JAS-D-21-0198.1.

kinetic energy generation to the convective mass flux increases by about 20% with an increase in the surface temperature of about 3.4 K. In summary, isentropic analysis extracts information about energy circulation directly from any three-dimensional datasets, separates the upward-moving, warm, and moist air from downward-moving, cold, and dry air, and isolates irreversible and reversible overturning because the equivalent potential temperature is constant in both dry and moist adiabatic processes. In this study, we used isentropic analysis to explore how surface heterogeneity and soil moisture gradients impact the energy transport in the boundary layer.

Atmospheric controls also impact the relationships between surface conditions and convection initiation [*Doran et al.*, 1995; *Findell and Eltahir*, 2003a; b; *Froidevaux et al.*, 2014; *Lee et al.*, 2019; *Santanello et al.*, 2018]. For example, *Chen et al.* [2020] isolated the effects of land surface by removing the horizontal wind, initial horizontal variabilities of air temperature, pressure, and water vapor, and the temporal variabilities of water vapor from initial and boundary forcings to investigate the impact of large-scale advection on the interpretation of land-atmosphere interactions. They found that large-scale advection moves the shallow clouds formed over the dry soil regions in the morning to wet soil regions where rain is initiated in the early afternoon. In the absence of large-scale advection, convective clouds tend to stay over dry regions and rain out. In addition, large-scale advection also affects mesoscale circulations by damping [*Lee et al.*, 2019] or modifying [*Kim et al.*, 2004; *Prabha et al.*, 2007] secondary circulation. Thus, large-scale advection disrupts (or, at the minimum, obscures) local soil moisture-precipitation feedbacks.

This study aims to better understand the impact of surface heterogeneity on the energy redistribution during the formation of non-precipitating shallow clouds, which affects their ability to transition to deeper, precipitating convection later in the day. To isolate local effects,

Accepted for publication in *Journal of the Atmospheric Sciences*. DOI 10.1175/JAS-D-21-0198.1.

we used the same semi-realistic modeling method as *Chen et al.* [2020] with realistic land properties and modified meteorological forcing (See details in Section 2.2). *Chen et al.* [2020] identified six clusters with various timing and location of convection initiation events. They found that the convection initially starts over regions with the highest sensible heat flux associated with high sensible and low latent heat fluxes. In contrast, this research focuses on the vertical transport of energy and how land heterogeneity impacts transport. Using isentropic analysis, we showed that high sensible heat flux regions are associated with relatively high vertical velocity near the surface, and high latent heat flux regions are associated with relatively high moist energy in Section 3. The mixing of parcels rising from these two regions results in the formation of shallow clouds. We also assessed the impacts of soil moisture gradients on energy transport. In Section 2, we provided an overview of the case study and model configurations. Section 3 examines the cloud population distribution on isentropic coordinates to illustrate vertical energy transport relative to convection above the heterogeneous surface, the dominant spatial scales of energy transport in the atmosphere, and the sensitivity of the soil moisture gradient on energy transport and cloud populations. Section 4 presents the conclusions and discussions.

2. Methods

a. Overview of the case study and related modeling studies

The HI-SCALE field campaign [*Fast et al.*, 2019a] provided measurements to understand the life cycle of shallow clouds by coupling measurements of cloud macrophysical and microphysical properties to land surface properties, ecosystems, and aerosols. This study focuses on the case 30 August 2016 day, wherein shallow cumuli transitioned to cumulus congestus and deep convection during the afternoon). On that day, clouds were associated with a trough of low pressure that propagated from New Mexico to

Accepted for publication in *Journal of the Atmospheric Sciences*. DOI 10.1175/JAS-D-21-0198.1.

western Kansas, and clear-sky conditions prevailed over most of eastern Oklahoma and southeastern Kansas in the early morning (Figures 1a-b). In the late morning, shallow cumulus clouds formed. Some of those shallow cumuli transitioned to cumulus congestus and deep convection during the afternoon (Figure 1c). Figures 1d-e show weak inhibition based on Convective Inhibition (CIN) and moderate instability based on Convective Available Potential Energy (CAPE) in the early morning. Our simulations used a configuration similar to *Fast et al.* [2019b], including an interactive land surface parameterization and a more spatially variable soil properties and land use type obtained by combining in-situ measurements and satellite data (shown in Figures 2a-c), because their study highlighted the role of soil moisture heterogeneity in the initiation of convection.

b. Design of the semi-idealized LES simulation with large-scale wind removed

In this study, the simulation domain included central Oklahoma and southern Kansas, and covers an area of 297x297 km^2 at 300 m horizontal grid spacing (i.e., the red box in Figures 1a-b). It had 304 vertical grid levels extending up to 16.2 km above mean sea level (MSL) with a constant 24-m grid spacing from near the surface up to 6.2 km MSL that gradually increases above that level. Four soil layers were used by the land surface parameterization in which the default surface vertical grid spacing of 0.1 m was changed to 0.01 m so that surface soil and atmospheric temperature fluctuations are coupled better at large eddy scales [Liu and Shao, 2013; Lohou and Patton, 2014]. Interactive Noah land-surface parameterization [*Chen and Dudhia*, 2001] used in this study allows the surface fluxes to vary spatially and temporally in response to atmospheric conditions. The simulation period was between 12:00 UTC on August 30th (i.e., 05:30 LST) and 00:00 UTC on August 31st (i.e., 17:30 LST).

The default WRF land property settings were refined to generate realistic conditions by modifying the soil temperature, soil moisture, and land use type (Figures 2a-c). The spatial

Accepted for publication in *Journal of the Atmospheric Sciences*. DOI 10.1175/JAS-D-21-0198.1.

distribution of the top-layer soil moisture was included in Figure 2a (i.e., the same as *Chen et al.* [2020]). Both ARM and Oklahoma Mesonet stations and Global Land Evaporation Amsterdam Model (GLEAM) satellite data were used to modify the spatial variations of soil moisture and soil temperature. Lake and river temperature were also replaced with the mean of the G-1 infrared thermometer measurements over the lake and river surfaces (301 K). In addition, we replaced the land use values derived from a 30- m National Land Cover Database for 2011 [*Yang et al.*, 2018]. Such settings enable realistic heterogeneities in surface fluxes and Bowen ratio (i.e., the ratio between surface sensible heat fluxes and latent heat fluxes), as shown in Figures 2d-f.

Large-scale advection plays an important role in the location of clouds by moving them away from where they formed (*Chen et al.* [2020]). To isolate energy circulations as impacted by land heterogeneity, we used the same semi-idealized simulation as *Chen et al.* [2020] but removed large-scale advection. To do so, we modified the initial and boundary conditions for meteorological variables from the National Center for Environmental Predication Final (FNL) operational model global tropospheric analysis [National Center for Environmental Prediction, 2000] by setting zonal and meridional wind speeds at the initial state and lateral boundaries to near-zero values (i.e., 0.001 m s-1). To inhibit geostrophic winds, geopotential height and air temperature were set to domain mean values. All of these modifications were done on isobaric surfaces. Because the surface wind speeds are small (see Figure 2 of *Chen et al.* [2020]), surface fluxes from the semi-idealized simulations are very close to those from the FNL forced simulation (not shown). More discussions about the impacts of large-scale advection on clouds can be found in Figure 4 of *Chen et al.* [2020].

3. Mechanisms of Land-atmosphere Interactions

a. Analysis of Moist Convection on Isentropic Coordinates

Accepted for publication in *Journal of the Atmospheric Sciences*. DOI 10.1175/JAS-D-21-0198.1.

Moist convection transports energy from the surface to the free troposphere by convective updrafts of moist and warm air parcels and by accompanying downdrafts of dry and cold air parcels. *Pauluis and Mrowiec* [2013] introduced the representation of convective overturning on isentropic coordinates in numerical models. This approach averages variables at isentropic slices (i.e., variables within a given equivalent potential temperature, θ_e, bin). They showed that isentropic analysis offers a robust definition of the convective mass transport and separates irreversible overturning circulations from reversible oscillations such as gravity waves. In this study, similar calculations are performed. As in *Pauluis and Mrowiec* [2013], mass flux was calculated based on Equation 1;

$$< \rho w > (z, \theta_{e0}) = \frac{1}{(t_2 - t_1) L_x L_y} \int_{t_1}^{t_2} \int_0^{L_x} \int_0^{L_y} \rho w \delta(\theta_e - \theta_{e0}) dx dy dt \tag{1}$$

where ρ is the air density, w is vertical velocity, z is the height, L_x and L_y are the horizontal dimensions of the domain, and the examined time period is between t_1 and t_2. The Dirac delta function $\delta(\theta_e - \theta_{e0})$ returns 1 when $\theta_{e0} - 0.25 < \theta_e \leq \theta_{e0} + 0.25$ and 0 elsewhere, representing the conditioning "ρw" on each isentropic slice with values of θ_e belongs to the bin with the center value as θ_{e0} (i.e., 60 θ_{e0} bins from 330 to 360 K with a bin width of 0.5 K). Therefore, the horizontal two dimensions are reduced into one θ_e dimension. In Figure 3a, the isentropic distribution of mass flux integrated from 6:00 to 12:00 LST shows that convection starts with higher values of θ_e (i.e., red shadings), and the compensating downdrafts are associated with lower values of θ_e (i.e., blue shadings), confirming that isentropic analysis separates the updraft warm moist air and downdraft cold and dry as expected. Hereafter, "high θ_e" refers to the upward mass flux region with high values of θ_e (i.e., red colors in Figure 3a) and "low θ_e" refers to the downward mass flux region with low θ_e (i.e., blue colors in Figure 3a).

Accepted for publication in *Journal of the Atmospheric Sciences*. DOI 10.1175/JAS-D-21-0198.1.

Both potential temperature (θ) and water vapor mixing ratio (q_v) determine the values of θ_e. These two factors integrated from 6:00 LST to 12:00 LST are presented in Figures 3b-c to show the thermal instability and moisture associated with upward "high θ_e" and downward "low θ_e." Hydrometeor mixing ratios are also presented in Figures 3d-f to show their distribution on isentropic coordinates. The calculations of those specific variables in Figures 3b-f on the isentropic coordinate follow Equation 2,

$$< x > (z, \theta_{e0}) = \int_{t_1}^{t_2} \int_0^{L_x} \int_0^{L_y} x\rho\delta(\theta_e - \theta_{e0}) dxdydt / \int_{t_1}^{t_2} \int_0^{L_x} \int_0^{L_y} \rho\delta(\theta_e - \theta_{e0}) dxdydt \quad \textbf{(2)}$$

where x represents the specific variable under consideration. The dash-dot lines from Figures 3a-c are the domain-mean values of θ_e. The decreasing trends of domain-mean θ_e with increasing heights (up to ~650 hPa) represent the rapid decrease of moisture. Small variations of domain mean θ_e in the lower atmosphere (i.e., > 800 hPa) indicate the turbulent mixing in the boundary layer. The solid black lines separate the updraft from the downdraft in isentropic coordinates. The dotted lines represent the inflection lines based on θ, which include the points when the first derivative of θ to θ_e changes the sign (see details below). The white contour in Figure 3b marks the lowest 2% value of θ to show the instability close to the surface. Solar heating at the surface maintains the unstable stratifications of θ and further contributes to convection (Figure 3b). Below about 800 hPa, the values of θ_e mainly depends on q_v than θ. Clouds form above 900hPa. Inflection lines (i.e., the dotted lines in Figures 3b-c) are observed in both isentropic q_v and T, indicating the saturation on the high θ_e region (i.e., to the right of the inflection line), where condensation removes the water vapor and releases latent heating. Those results on isentropic coordinates are generally consistent with *Pauluis and Mrowiec* [2013] that upward transportation of energy is separated from the downward ones. The following paragraphs show how those upward and downward transportations relate to land surface heterogeneity.

To link those isentropic distributions of cloud and meteorological properties with land heterogeneity, we explored the surface moisture, surface fluxes, and cloud water path associated with "high θ_e" and "low θ_e" close to the surface (~30 m above ground) and at the cloud altitudes (i.e., ~3 km above ground level/ 700 hPa) at 12:00 LST when the surface fluxes are large (Figures 4c-d). Dots on the line together account for 99.9% of model grids. Squares represent cloud water path greater than 0.045 kg m^{-2} that would significantly reduce downwelling radiation reaching the surface by cloud shading (i.e., the cloud shading effect is strong enough to cause the opposite trends in surface sensible heat flux in Figure 4c). The dashed lines in Figure 4b show the soil moisture at 8:00 LST, which excludes the impacts of the light precipitation on soil moisture in the morning. The solid and dashed lines are quite similar, suggesting that the precipitation does not significantly affect surface soil moisture during the morning. The cloud water path has large values on low near-surface θ_e (blue lines in Figure 4a); Sensible heat flux is larger (drier soil) with lower near-surface θ_e (i.e., blue arrow in Figure 4c) except those impacted significantly by cloud shading denoted by squares, while latent heat flux is larger (wetter soil) with higher θ_e. Except for those impacted by cloud shading, high θ_e at ~ 3 km (i.e., orange lines) are associated with high sensible heat (i.e., orange arrow in Figure 4c), low latent heat, dry soil, and high cloud water path.

The opposite trends of land properties and θ_e at different altitudes shown in Figure 4 imply a "dipole" spatial structure of θ_e. By considering the consistent relationships between w and θ_e at all altitudes, the "dipole" structure suggests that a heterogeneous surface generates circulation to transport energy horizontally in the boundary layer. Upward transport of energy (i.e., high θ_e) starts over the surface regions with high latent heat, low sensible heat, and moist

File generated with AMS Word template 1.0

Accepted for publication in *Journal of the Atmospheric Sciences*. DOI 10.1175/JAS-D-21-0198.1.

soil. Those parcels with high energy near the surface end up at higher altitudes over regions with low latent heat, high sensible heat, and dry soil (e.g., 3 km).

b. Interpretation in the context of previous studies

Previous studies usually indicated that convection initiates over high sensible heat regions (e.g., *Kang and Bryan* [2011]; *Rieck et al.* [2015]), different from what we saw using isentropic analysis (i.e., compositing datasets by θ_e) where upward motion (associated with high θ_e) initiates over high latent heat flux (wet soil) regions. To better understand this conclusion based on the isentropic analysis described in Section 3.a and explain the differences from those previous results, we composited data by Bowen ratio in Figure 5, as many previous studies did, at 10:00 LST about 30 min after clouds start to form. Compositing by the Bowen ratio separates the wet patches from the dry patches and can directly illustrate the location of the convection initiation. The Bowen ratio is averaged between 7:30 and 8:30 LST to focus on the initial effect of soil moisture and exclude the effects of cloud shading and precipitation. The cloud water mixing ratio, shown by color shading in Figures 5a-b, confirms that the clouds initiate over high sensible heat flux regions. Instantaneous θ_e anomalies (i.e., removing domain-mean values) suggest transportation of high θ_e anomalies from low Bowen ratio regions near the surface to high Bowen ratio near sub-cloud layers (i.e., black arrows in Figure 5a). Such transport explains why high θ_e anomalies are associated with low Bowen ratio near the surface in the isentropic analysis.

To compare our simulated circulations with previous studies (e.g., *Kang and Bryan* [2011]; *Rieck et al.* [2015]), we also showed the circulations at each Bowen ratio bin (i.e., roughly at mesoscale) in Figures 5b-d. Larger positive vertical velocities occur above high Bowen ratio regions (Figure 5b). Within a few hundred meters above the surface, the divergence of air and moisture (i.e., positive values) occurs more frequently over locations with low Bowen ratio,

Accepted for publication in *Journal of the Atmospheric Sciences*. DOI 10.1175/JAS-D-21-0198.1.

and convergence (i.e., negative values) occurs over locations of the high Bowen ratio, indicating a net flow from low to high Bowen ratio regions (i.e., black arrows) (Figures 5c-d). The divergence regions are lifted from over low Bowen ratio regions to over the high Bowen ratio regions. Thus, the mesoscale circulation depicted in Figures 5b-c shows that upward motion and convergence are above dryer soil (high Bowen ratio regions), and downward motions and divergence occur over wetter soil (low Bowen ratio regions), which is consistent with the findings of previous studies.

We also examined the relationships between w and θ_e using partial differentiation as follows:

$$\frac{dw}{d\theta_e} = \left.\frac{\partial w}{\partial \theta_e}\right|_{BR} + \frac{\partial w}{\partial BR}\frac{\partial BR}{\partial \theta_e} \qquad \textbf{(3)}$$

where BR is the Bowen ratio. The first term on the right side of Equation 3 represents the direct relationships between w and θ_e close to the surface with a fixed Bowen ratio. Positive relationships between w and θ_e in Figures 6a-c suggest that, with a fixed Bowen ratio, air parcels with more moist static energy (i.e., θ_e) are associated stronger updrafts. The second term on the right side represents the indirect relationships between θ_e and w via the intermediate variable BR (Figure 6d). Small values of the slope in Figure 6d suggest weak relationships between w and θ_e via the Bowen ratio. The slightly negative relationships come from the negative relationship between the Bowen ratio and θ_e (not shown), which leads to high w and low θ_e over the same locations as the high Bowen ratio near the surface shown in Figure 5. Figures 6a-c confirm the results from Figures 3-4 that stronger updrafts correspond to air parcels with higher moist static energy, and Figure 6d agrees with Figure 5 that positive w corresponds to slightly lower θ_e when binned by Bowen ratio.

Accepted for publication in *Journal of the Atmospheric Sciences*. DOI 10.1175/JAS-D-21-0198.1.

Then, we also examined the relationships between w and BR in Equation 4 below to support our understanding of the mesoscale circulation shown in Figures 5b-d.

$$\frac{dw}{dBR} = \left.\frac{\partial w}{\partial BR}\right|_{\theta_e} + \frac{\partial w}{\partial \theta_e}\frac{\partial \theta_e}{\partial BR} \quad \textbf{(4)}$$

Figures 6e-g indicate that the direct relationships between the Bowen ratio and w (i.e., the first term on the right side of Equation 4) are mostly positive, especially when w is positive because high sensible heat increases a parcel's buoyancy. Figure 6h and the second term on the right side of Equation 4 indicate that in each θ_e (i.e., energy) bin Bowen ratio negatively relates to w and large θ_e relates to high w. Large absolute value of the slope of linear regression suggests the relationship between Bowen ratio and w via θ_e is strong. Figures 6e-g are consistent with Figure 5 that positive w corresponds to a higher Bowen ratio. Figure 6h is consistent with Figures 3-4 that positive w corresponds to lower sensible heat flux and higher latent heat flux close to the surface (i.e., low Bowen ratio). Also, the above analysis shows the moist static energy (θ_e) largely changes the relationships between w and BR, but BR does not have a significant effect on the relationships between w and θ_e.

The stronger relationships between w and θ_e than those between w and Bowen ratio can also be observed in the larger range of w values when binned by θ_e than by Bowen ratio in Figures 6d and 6h (w spanning a wider range in the y-axis), and the separation of updraft and downdraft by the highest and lowest 2% values of θ_e (Figures 6e and 6g).

To understand why there is a relatively stronger relationship between w and θ_e close to the surface, we examined the moving averaged covariance between w, θ_e and Bowen ratio in Figures 7a-c (i.e., $COV(var1, var2) = (var1 - \overline{var1})(var2 - \overline{var2})$). Moving averages (i.e., moving mean or rolling mean) is a calculation to average the datasets in different subsets of the full datasets that the centers of the subsets traverse within the domain. Each subset covers

Accepted for publication in *Journal of the Atmospheric Sciences*. DOI 10.1175/JAS-D-21-0198.1.

the data spatially around. The moving standard deviation mentioned below is the standard deviation of the subsets. Larger absolute values of $COV(var1, var2)$ denote stronger relationships between the two variables. We performed the covariance analysis on the moving averaged values to filter out the noise below the mesoscale (here chosen to be 27 km). As shown in Figure 7, positive values in $COV(w, \theta_e)$ over most of the domain confirms the strong positive relationships between w and θ_e. The small (i.e., less than 0.01) absolute values of $COV(w, BR)$ over most of the domain in Figure 7b indicate that BR does not directly influence w. The small patches with large values in Figure 7b are due to a large moving standard deviation of BR (Figure 7i). The absolute values of $COV(\theta_e, BR)$ in Figure 6c are large when the moving averaged values of BR are large (Figure 7f), which means BR impacts θ_e largely when BR is large. The black contours in Figure 7 denote the 100 W m^{-2} contour of surface sensible heat flux, and the area inside the black circles has values larger than 100 W m^{-2}, so the high BR is more tightly related to high sensible heat (i.e., low latent heat). Thus, along with Figure 6g showing that high θ_e is over a high latent heat region, the turbulent updraft over a high latent heat region likely contributes to high values of θ_e, which explains the tight relationships between upward mass flux and positive θ_e anomalies over high latent heat region in the isentropic analysis. When the data are binned by the Bowen ratio, those turbulent variations of w and θ_e are smoothed; thus, Figure 5 with the compositing by BR shows opposite relationships than those in the isentropic analysis from Figures 3 and 4. Note that the above analysis does not suggest that the relationships shown in Figure 5 are not robust. Comparing Figures 7g-i also indicate that the spatial variations of the Bowen ratio are at larger spatial lengths than the variations of w and θ_e due to the smaller moving deviation of BR except for the edges of high BR patches. These contrasting relationships reveal different phenomena occurring at different scales.

Accepted for publication in *Journal of the Atmospheric Sciences*. DOI 10.1175/JAS-D-21-0198.1.

To quantify the energy transport over different Bowen ratio regions, Figure 8 shows the isentropic analysis of mass flux for five Bowen ratio bins. Figure 8f and Figures 8a-e separate the mass flux by the averaged ones at each Bowen ratio bin and the anomalies with respect to the composite mean. With increasing Bowen ratio, the zero-mass flux line moves to lower values of θ_e, the magnitude of mass flux increases, and the vertical extent of the transport reaches higher. Note that the variation above 850 hPa in Figure 8e might indicate turbulent entrainment-mixing within the cloud layer. The averaged mass flux at Bowen ratio bins is much smaller than the anomalies of mass flux. Figure 8 also implicitly reveals the spatial scale separation because Bowen ratio variations in this study are mainly at the mesoscale (the size of soil moisture patches is roughly 30 km in Figure 2a).

To summarize the circulation based on isentropic and composite analysis by Bowen ratio, Figure 9 conditionally averages w by their sign so that the large turbulence will be reflected on the values of the arrows. With increasing Bowen ratio (i.e., at around mesoscale), net vertical velocity increases (Figure 5b) while θ_e in the air parcels decreases (Figure 5a). The horizontal variations of θ_e are mainly associated with water vapor (Figure 3b-c). Thus, over high latent heat regions (i.e., low BR), the net transport of θ_e (i.e., water vapor) is higher than over high sensible heat regions due to stronger evapotranspiration. High w results in the upward transport of θ_e from the ground surface into the atmosphere. Clouds form as air parcels with high w ascending from high sensible heat regions and mix with those with high θ_e ascending from high latent heat regions. The mixing can be inferred by the convergence shown in yellow-green shading in Figure 9.

Figure 10 shows the joint probability density function of w and θ_e close to the surface and below the cloud base at 10:00 LST. Cloud water path is high over locations with low θ_e at ~30m, however at ~1000 m (i.e., 870 hPa, just below cloud base), clouds are over higher θ_e

Accepted for publication in *Journal of the Atmospheric Sciences*. DOI 10.1175/JAS-D-21-0198.1.

and high absolute values of w, indicating a mixing process between the air parcels starting from different locations with different surface energy partitions.

c. Quantifying the Scale-Dependent Transport of Energy

In *Chen et al.* [2020], the authors used cluster analysis to classify the temporal and vertical distributions of θ_e into 6 clusters where each cluster has a unique convective feature in terms of timing, location, and intensity of convection. Cluster analysis was used because the realistic land properties are complex with various soil moisture patch sizes and different combinations of soil moisture, land use type and soil type. They showed that the location of each cluster is influenced by land properties, including soil moisture, land use type, and soil type. The specific two out of six clusters corresponding to the earliest convection are over the high sensible heat region, which is consistent with the mesoscale circulation shown in Figure 5a. The isentropic analysis in Section 3.a suggests the rising parcels with higher values of θ_e are located above low sensible heat regions, and the sinking parcels with lower values of θ_e are located over high sensible heat flux regions. As shown in Figure 6a-d, the strong relationship between w and θ_e is noisy at each Bowen ratio bin (i.e., ~mesoscale) and suggests that land-heterogeneity-induced convective circulations are different at mesoscale and sub-mesoscale (e.g., *Kang and Ryu* [2016]; *Williams et al.* [2020]).

In terms of the comparative contributions of vertical transport of energy at different scales in the same case, we continued to use the cluster identified by *Chen et al.* [2020] in Figure 11 to show the mean values and anomalies of the vertical transport of θ_e for different Bowen ration at the cluster and sub-cluster scales, respectively, that are defined by:

$$x = \bar{x} + x'_{cl} + x'_{sub} \quad \textbf{(5)}$$

Accepted for publication in *Journal of the Atmospheric Sciences*. DOI 10.1175/JAS-D-21-0198.1.

where $\bar{x}$ is domain-mean values, x'_{cl} is the cluster-mean values after the domain-mean values are subtracted, while x'_{sub} is the sub-cluster scale. Here Bowen ratio is averaged from 7:30 to 8:30 LST (i.e., in the same way as Figure 5). Cluster-scale circulation, which is roughly at mesoscale, plays a minor role in the vertical transport of energy while sub-cluster scale circulation dominates transportation (note the difference in magnitude between Figure 11a and 11b). The domain mean values of the cross-product term ($\overline{w'_{cl}\theta'_{e,sub}}$ and $\overline{w'_{sub}\theta'_{e,cl}}$) are 1 to 2 orders smaller than the transport at cluster scale (not shown).

Cluster analysis provides useful information about the multi-scale behaviors over the land with different Bowen ratios. However, the spatial size of the cluster is not easy to estimate. Analysis of mass flux on isentropic coordinates naturally reveals the vertical transport of energy because those oscillations without energy transport are compensated, such as those data points with θ_e along the zero net mass flux in Figure 3a. Here we decomposed the mass flux at isentropic coordinates into multiple scales at 270 km (i.e., domain mean), 27-270 km, 2.7-27 km, and 0.3-2.7 km to isolate the contributions from various spatial scales and provide an estimate of the length scale of multi-scale behaviors. Mass flux at 27-270 km is the averaged value at each 27×27 km^2 sub-regions after removing domain mean values, while mass flux at 2.7-27 km is the averaged value at each 2.7×2.7 km^2 sub-regions after removing the domain mean and the values at 27-270 km. The residuals are the mass flux at 0.3-2.7 km. Figure 12 shows the isentropic distribution of mass flux associated with multiple scales averaged and integrated from 6:00 to 12:00 LST, note that θ_e are not decomposed. At scales between 27-270 km, updrafts in low troposphere are not associated with high θ_e and do not account for energy transport, while upward mass flux above a few hundred meters is associated with high θ_e and contributes to energy transport. The upward energy transport below a few hundred meters occurs at scales less than 27 km. At scales between 2.7-27 km, both the vertical extent of

Accepted for publication in *Journal of the Atmospheric Sciences*. DOI 10.1175/JAS-D-21-0198.1.

circulation and the horizontal variations of θ_e is smaller than those between 0.3-2.7 km, suggesting a dominant role of sub-mesoscale eddies in the upward energy transport from the surface to the atmosphere. Here both cluster analysis and isentropic analysis at different scales show that the energy transport between land and the lower boundary layer is dominant in the sub-mesoscale.

d. Impacts of soil moisture gradient

To investigate the impacts of the initial soil moisture gradient on cloud formation and energy transport, we conducted two sensitivity simulations in addition to the control simulation (hereafter "obsSM”). One of them is with uniform soil moisture (hereafter “uniSM”), and the other has a similar pattern of initial soil moisture to “obsSM” except that the spatial gradient is larger (hereafter “larSM”). Figure A1 shows the spatial pattern of the initial soil moisture of the three simulations. Figure 13 shows the isentropic distribution of the liquid water mixing ratio integrated at 11:00 LST. The increases in cloud depth and precipitation appear to be related to more vigorous energy transport associated with the larger spatial gradient in the initial soil moisture.

Figure 14 explores the impacts of soil moisture gradient on energy transport at different spatial scales at 10:30 before precipitation onset for all three simulations. In each panel, the domain-mean and standard deviation of the vertical transport of θ_e (Figures 14a, 14c and 14d) and horizontal divergence (Figures 14b, 14d and 14f) is shown. For all three simulations, upward vertical transport from the surface up to the cloud base occurs at scales smaller than 27 km (i.e., positive values below ~900 hPa, solid lines in Figures 14c and 14e). At scales between 27-270 km, downward transport occurs in the lower boundary layer while upward transport occurs above the boundary layer (solid lines in Figure 14a). These results are consistent with Figure 12. Large soil moisture gradients contribute to large upward transport of energy at high

Accepted for publication in *Journal of the Atmospheric Sciences*. DOI 10.1175/JAS-D-21-0198.1.

altitudes (solid lines in Figure 14a), large convergence at scales between 27-270 km (solid lines in Figure 14b), large divergence at scales between 2.7-27 km (solid lines in Figure 14d), and large spatial variations of both vertical transport and horizontal divergence occurs at all spatial scales (dashed lines in Figure 14). The large impact of soil moisture gradient on the horizontal divergence at scales between 27-270 km is likely due to the similar size of soil moisture patches, which has a mean equivalent radius of 30 km based on the watershed classification (Figure 2a).

4. Discussion

This study focuses on the morning period with shallow clouds forming during clear-sky conditions. During the afternoon, convection is also likely to be influenced by land heterogeneity, but precipitation and moving cloud systems obscure our analysis. The vertical profiles of temperature and humidity (Figures 1d-e) show weak inhibition based on Convective Inhibition (CIN) and moderate instability based on Convective Available Potential Energy (CAPE) in the early morning, and the large-scale advection is removed in the initial and boundary forcing. Thus, energy transport under a wide range of thermodynamic and wind conditions is not examined by this study.

Some studies demonstrated that even modest background winds (e.g., > 2 m/s in *Lee et al. [2019]*) can effectively eliminate the impacts of surface heterogeneity or modify secondary circulations [e.g., *Kim et al.*, 2004; *Prabha et al.*, 2007]. Therefore, the isentropes in this study might be moved under different wind conditions. Further, cloud development relative to mesoscale flow patterns is sensitive to the amount of CIN in the local environment *[Garcia-Carreras et al. 2011]*. Also, the different conditions of the surface heterogeneity, including the size of soil moisture patches and domain mean soil moisture conditions, might influence the isentropes and the location of the clouds. We also noted that the present analysis used a soil

Accepted for publication in *Journal of the Atmospheric Sciences*. DOI 10.1175/JAS-D-21-0198.1.

moisture distribution that has a variability at a scale that is likely larger than reality (i.e., smoothed at about mesoscale). Therefore, generalizing our conclusions to a wider variety of CIN, CAPE, wind conditions, and soil moisture variation scales warrants future investigation.

5. Summary

In this study, we examined energy transport associated with surface heterogeneity induced moist convection on isentropic coordinates. We conducted Large Eddy Simulations using the Weather Research and Forecasting model coupled with an interactive land model, with large-scale the background wind removed to isolate the role of the surface heterogeneity. August 30th, 2016, during the HI-SCALE field campaign near the ARM Southern Great Plains site in north-central Oklahoma, was selected as a case study. In contrast to previous studies that usually employ simple soil moisture gradients, we used spatially varying soil moisture distributions based on observed conditions for that day. This study also employs isentropic coordinate analyses to better understand land-atmosphere interactions influenced by these variable soil moisture distributions. We explored the scale dependence of the relationships among vertical velocity (w), equivalent potential temperature (θ_e), and Bowen ratio and showed that the sub-mesoscale flow plays the dominant role in the vertical transport of energy near the surface compared to mesoscale flow.

Analysis on isentropic coordinates shows that convective updrafts and formation of clouds take place over columns with high values of θ_e, while downdrafts and surface precipitation are located over the columns with low values θ_e. Close to the surface, high θ_e is correlated with low values of sensible heat fluxes, high values of latent heat fluxes, moist soil, and low values of the cloud water path. However, an opposite pattern was found near cloud base, at about 3 km. The schematic diagram in Figure 9 illustrates the transport of energy. Ascending air parcels have higher vertical velocities over locations with high sensible heat flux, while air parcels

Accepted for publication in *Journal of the Atmospheric Sciences*. DOI 10.1175/JAS-D-21-0198.1.

over locations with high latent heat flux have higher moist energy (i.e., θ_e). Even though updrafts are usually above locations with high sensible heat flux, the moist parcels start over high latent heat regions at sub-mesoscale (i.e., smaller than surface heterogeneity size of about 30.6 km). Those high moist energy parcels are converged horizontally towards regions with high sensible heat flux directly below the cloud base. Clouds form as the high vertical velocity and high moist energy air mix. Above new mechanism shown by isentropic framework explains how soil moisture heterogeneity provides the key ingredients such as buoyancy and moisture for shallow cloud formation.

The relationships among three key variables (i.e., near-surface w, near-surface θ_e, and Bowen ratio) were examined by considering the relationship between two of them at one time while the third was kept constant. The relationships between w and θ_e are stronger than that between w and the Bowen ratio. Also, spatial variations of w and θ_e are at sub-mesoscale mixing scales while variations of Bowen ratio are at the mesoscale as it is related to the soil moisture variability. Thus, we examined energy transport at multiple spatial scales. Spatial scales smaller than the mesoscale plays the dominant role in the net upward transport of energy in the boundary layer. The isentropic analysis at multiple spatial scales also shows that energy circulation at scales larger than 27 km does not significantly contribute to the transport of surface energy within the boundary layer. However, that scale contributes to vertical energy transport above the boundary layer.

Moreover, we examined the impact of initial soil moisture gradients on energy transport by comparing three simulations with the same values of domain-mean soil moisture (i.e., 0.23 kg kg^{-1}) but with different gradients with no large-scale forcing. Larger soil moisture gradients are associated with more vigorous energy transport and stronger mixing of the two different kinds of air parcels ascending from the surface with different energy partitions discussed above. In a

Accepted for publication in *Journal of the Atmospheric Sciences*. DOI 10.1175/JAS-D-21-0198.1.

similar study but based on 7-years observation data over the Southern Great Plains, *Frye and Mote* [2010] found that increased soil moisture gradient values are associated with decreased convection initiation to a point. However, the likelihood of convection initiation increases after soil moisture reaches 15% with a low-level jet, or 25% without one. The positive relationships between convection and soil moisture gradient in our study are related to the relatively high values of mean soil moisture. We also found that horizontal wind divergence at 27-270 km is most sensitive to soil moisture gradient, likely due to the similar scale of soil moisture patches. That finding for a realistic soil moisture distribution agrees with previous idealized modeling studies that show surface heterogeneity patch-induced secondary circulation is at a comparable size to the soil moisture patches [*Lee et al.*, 2019; *Patton et al.*, 2005].

While we have demonstrated that isentropic analysis is a useful tool to illustrate land-atmosphere interactions, generalizing our conclusions to a wider variety of CIN, CAPE, wind conditions, and soil moisture variation scales warrants further investigations.

Acknowledgments.

This study is supported by the U.S. Department of Energy Office of Science Biological and Environmental Research as part of the Atmospheric Systems Research (ASR) Program. The modeling studies were supported by the Environmental Molecular Science Laboratory's (EMSL) Cascade computational cluster. Pacific Northwest National Laboratory is operated by Battelle for the U.S. Department of Energy under Contract DE-AC05-76RLO1830. We also thank Dr. Olivier Paulius for discussing aspects of isentropic analysis used in this study.

Data Availability Statement.

Accepted for publication in *Journal of the Atmospheric Sciences*. DOI 10.1175/JAS-D-21-0198.1.

The WRF community model was made available from the National Center for Atmospheric Research (NCAR) at http://www2.mmm.ucar.edu/wrf/users/. Approximately 10 Tb of WRF model output was generated by the simulations in this study, which are saved on the long- term storage system at PNNL.

REFERENCES

Avissar, R., and Y. Liu (1996), Three-dimensional numerical study of shallow convective clouds and precipitation induced by land surface forcing, *Journal of Geophysical Research: Atmospheres*, *101*(D3), 7499-7518, doi:10.1029/95jd03031.

Avissar, R., and T. Schmidt (1998), An Evaluation of the Scale at which Ground-Surface Heat Flux Patchiness Affects the Convective Boundary Layer Using Large-Eddy Simulations, *Journal of the Atmospheric Sciences*, *55*(16), 2666-2689, doi:10.1175/1520-0469(1998).

Chen, F., and J. Dudhia (2001), Coupling an Advanced Land Surface–Hydrology Model with the Penn State–NCAR MM5 Modeling System. Part I: Model Implementation and Sensitivity, *Monthly Weather Review*, *129*(4), 569-585, doi:10.1175/1520-0493(2001)129<0569:Caalsh>2.0.Co;2.

Chen, J., S. Hagos, H. Xiao, J. D. Fast, and Z. Feng (2020), Characterization of Surface Heterogeneity-Induced Convection Using Cluster Analysis, *Journal of Geophysical Research: Atmospheres*, *125*(20), e2020JD032550, doi:https://doi.org/10.1029/2020JD032550.

Accepted for publication in *Journal of the Atmospheric Sciences*. DOI 10.1175/JAS-D-21-0198.1.

Chen, X., O. M. Pauluis, L. R. Leung, and F. Zhang (2018), Multiscale Atmospheric Overturning of the Indian Summer Monsoon as Seen through Isentropic Analysis, *Journal of the Atmospheric Sciences*, *75*(9), 3011-3030, doi:10.1175/jas-d-18-0068.1.

Dai, A., F. Giorgi, and K. E. Trenberth (1999), Observed and model-simulated diurnal cycles of precipitation over the contiguous United States, *Journal of Geophysical Research: Atmospheres*, *104*(D6), 6377-6402, doi:10.1029/98jd02720.

Doran, J. C., W. J. Shaw, and J. M. Hubbe (1995), Boundary Layer Characteristics over Areas of Inhomogeneous Surface Fluxes, *Journal of Applied Meteorology*, *34*(2), 559-571, doi:10.1175/1520-0450-34.2.559.

Fast, J. D., et al. (2019a), Overview of the HI-SCALE Field Campaign: A New Perspective on Shallow Convective Clouds, *Bulletin of the American Meteorological Society*, *100*(5), 821-840, doi:10.1175/bams-d-18-0030.1.

Fast, J. D., L. K. Berg, Z. Feng, F. Mei, R. Newsom, K. Sakaguchi, and H. Xiao (2019b), The Impact of Variable Land-Atmosphere Coupling on Convective Cloud Populations Observed During the 2016 HI-SCALE Field Campaign, *Journal of Advances in Modeling Earth Systems*, *0*(0), doi:10.1029/2019ms001727.

Findell, K. L., and E. A. B. Eltahir (2003a), Atmospheric Controls on Soil Moisture–Boundary Layer Interactions. Part I: Framework Development, *Journal of Hydrometeorology*, *4*(3), 552-569, doi:10.1175/1525-7541(2003).

Findell, K. L., and E. A. B. Eltahir (2003b), Atmospheric Controls on Soil Moisture–Boundary Layer Interactions. Part II: Feedbacks within the Continental United States, *Journal of Hydrometeorology*, *4*(3), 570-583, doi:10.1175/1525-7541(2003)004.

Accepted for publication in *Journal of the Atmospheric Sciences*. DOI 10.1175/JAS-D-21-0198.1.

Froidevaux, P., L. Schlemmer, J. Schmidli, W. Langhans, and C. Schär (2014), Influence of the Background Wind on the Local Soil Moisture–Precipitation Feedback, *Journal of the Atmospheric Sciences*, *71*(2), 782-799, doi:10.1175/jas-d-13-0180.1.

Frye, J. D., and T. L. Mote (2010), Convection Initiation along Soil Moisture Boundaries in the Southern Great Plains, *Monthly Weather Review*, *138*(4), 1140-1151, doi:10.1175/2009mwr2865.1.

Garcia-Carreras, L., D. J. Parker, and J. H. Marsham (2011), What is the Mechanism for the Modification of Convective Cloud Distributions by Land Surface–Induced Flows?, *Journal of the Atmospheric Sciences*, *68*(3), 619-634, doi:10.1175/2010jas3604.1.

Gentine, P., A. A. M. Holtslag, F. D'Andrea, and M. Ek (2013), Surface and Atmospheric Controls on the Onset of Moist Convection over Land, *Journal of Hydrometeorology*, *14*(5), 1443-1462, doi:10.1175/jhm-d-12-0137.1.

Hadfield, M. G., W. R. Cotton, and R. A. Pielke (1991), Large-eddy simulations of thermally forced circulations in the convective boundary layer. Part I: A small-scale circulation with zero wind, *Boundary-Layer Meteorology*, *57*(1), 79-114, doi:10.1007/BF00119714.

Huang, H.-Y., and S. A. Margulis (2013), Impact of soil moisture heterogeneity length scale and gradients on daytime coupled land-cloudy boundary layer interactions, *Hydrological Processes*, *27*(14), 1988-2003, doi:10.1002/hyp.9351.

Kang, S.-L. (2016), Regional Bowen ratio controls on afternoon moist convection: A large eddy simulation study, *Journal of Geophysical Research: Atmospheres*, *121*(23), 14,056-014,083, doi:10.1002/2016jd025567.

Accepted for publication in *Journal of the Atmospheric Sciences*. DOI 10.1175/JAS-D-21-0198.1.

Kang, S.-L., and G. H. Bryan (2011), A Large-Eddy Simulation Study of Moist Convection Initiation over Heterogeneous Surface Fluxes, *Monthly Weather Review*, *139*(9), 2901-2917, doi:10.1175/mwr-d-10-05037.1.

Kang, S.-L., and J.-H. Ryu (2016), Response of moist convection to multi-scale surface flux heterogeneity, *Q. J. R. Meteorol. Soc.*, *142*(698), 2180-2193, doi:10.1002/qj.2811.

Kim, H.-J., Y. Noh, and S. Raasch (2004), Interaction between Wind and Temperature Fields in the Planetary Boundary Layer for a Spatially Heterogeneous Surface Heat Flux, *Boundary-Layer Meteorology*, *111*(2), 225-246, doi:10.1023/B:BOUN.0000016471.75325.75.

Lee, J. M., Y. Zhang, and S. A. Klein (2019), The Effect of Land Surface Heterogeneity and Background Wind on Shallow Cumulus Clouds and the Transition to Deeper Convection, *Journal of the Atmospheric Sciences*, *76*(2), 401-419, doi:10.1175/jas-d-18-0196.1.

Liu, S., and Y. Shao (2013), Soil-layer configuration requirement for large-eddy atmosphere and land surface coupled modeling, *Atmospheric Science Letters*, *14*(2), 112-117, doi:10.1002/asl2.426.

Lohou, F., and E. G. Patton (2014), Surface Energy Balance and Buoyancy Response to Shallow Cumulus Shading, *Journal of the Atmospheric Sciences*, *71*(2), 665-682, doi:10.1175/jas-d-13-0145.1.

McPherson, R. A. (2007), A review of vegetation—atmosphere interactions and their influences on mesoscale phenomena, *Progress in Physical Geography: Earth and Environment*, *31*(3), 261-285, doi:10.1177/0309133307079055.

Nesbitt, S. W., and E. J. Zipser (2003), The Diurnal Cycle of Rainfall and Convective Intensity according to Three Years of TRMM Measurements, *Journal of Climate*, *16*(10), 1456-1475, doi:10.1175/1520-0442(2003)016<1456:Tdcora>2.0.Co;2.

Accepted for publication in *Journal of the Atmospheric Sciences*. DOI 10.1175/JAS-D-21-0198.1.

Patton, E. G., P. P. Sullivan, and C.-H. Moeng (2005), The Influence of Idealized Heterogeneity on Wet and Dry Planetary Boundary Layers Coupled to the Land Surface, *Journal of the Atmospheric Sciences*, *62*(7), 2078-2097, doi:10.1175/jas3465.1.

Pauluis, O., and A. A. Mrowiec (2013), Isentropic Analysis of Convective Motions, *Journal of the Atmospheric Sciences*, *70*(11), 3673-3688, doi:10.1175/jas-d-12-0205.1.

Pauluis, O. M. (2016), The Mean Air Flow as Lagrangian Dynamics Approximation and Its Application to Moist Convection, *Journal of the Atmospheric Sciences*, *73*(11), 4407-4425, doi:10.1175/jas-d-15-0284.1.

Prabha, T. V., A. Karipot, and M. W. Binford (2007), Characteristics of secondary circulations over an inhomogeneous surface simulated with large-eddy simulation, *Boundary-Layer Meteorology*, *123*(2), 239-261, doi:10.1007/s10546-006-9137-6.

Randall, D. A., Harshvardhan, and D. A. Dazlich (1991), Diurnal Variability of the Hydrologic Cycle in a General Circulation Model, *Journal of the Atmospheric Sciences*, *48*(1), 40-62, doi:10.1175/1520-0469(1991)048<0040:Dvothc>2.0.Co;2.

Rieck, M., C. Hohenegger, and P. Gentine (2015), The effect of moist convection on thermally induced mesoscale circulations, *Q. J. R. Meteorol. Soc.*, *141*(691), 2418-2428, doi:https://doi.org/10.1002/qj.2532.

Rochetin, N., F. Couvreux, and F. Guichard (2017), Morphology of breeze circulations induced by surface flux heterogeneities and their impact on convection initiation, *Q. J. R. Meteorol. Soc.*, *143*(702), 463-478, doi:doi:10.1002/qj.2935.

Santanello, J. A. J., et al. (2018), Land–Atmosphere Interactions: The LoCo Perspective, *Bulletin of the American Meteorological Society*, *99*(6), 1253-1272, doi:10.1175/bams-d-17-0001.1.

Accepted for publication in *Journal of the Atmospheric Sciences*. DOI 10.1175/JAS-D-21-0198.1.

Segal, M., and R. W. Arritt (1992), Nonclassical Mesoscale Circulations Caused by Surface Sensible Heat-Flux Gradients, *Bulletin of the American Meteorological Society*, *73*(10), 1593-1604, doi:10.1175/1520-0477(1992)073.

Stevens, B. (2005), Atmospheric Moist Convection, *Annual Review of Earth and Planetary Sciences*, *33*(1), 605-643, doi:10.1146/annurev.earth.33.092203.122658.

Taylor, C. M., A. Gounou, F. Guichard, P. P. Harris, R. J. Ellis, F. Couvreux, and M. De Kauwe (2011), Frequency of Sahelian storm initiation enhanced over mesoscale soil-moisture patterns, *Nature Geoscience*, *4*, 430, doi:10.1038/ngeo1173.

Taylor, C. M., D. J. Parker, and P. P. Harris (2007), An observational case study of mesoscale atmospheric circulations induced by soil moisture, *Geophysical Research Letters*, *34*(15), doi:10.1029/2007gl030572.

Wallace, J. M. (1975), Diurnal Variations in Precipitation and Thunderstorm Frequency over the Conterminous United States, *Monthly Weather Review*, *103*(5), 406-419, doi:10.1175/1520-0493(1975)103<0406:Dvipat>2.0.Co;2.

Williams, I. N., J. M. Lee, J. Tadić, Y. Zhang, and H. Chu (2020), Modeling spatial heterogeneity in surface turbulent heat flux in the US Southern Great Plains, *Journal of Geophysical Research: Atmospheres*, *n/a*(n/a), e2019JD032255, doi:10.1029/2019jd032255.

Wu, C.-M., M.-H. Lo, W.-T. Chen, and C.-T. Lu (2015), The impacts of heterogeneous land surface fluxes on the diurnal cycle precipitation: A framework for improving the GCM representation of land-atmosphere interactions, *Journal of Geophysical Research: Atmospheres*, *120*(9), 3714-3727, doi:10.1002/2014jd023030.

File generated with AMS Word template 1.0

Accepted for publication in *Journal of the Atmospheric Sciences*. DOI 10.1175/JAS-D-21-0198.1.

Yang, L., et al. (2018), A new generation of the United States National Land Cover Database: Requirements, research priorities, design, and implementation strategies, *ISPRS Journal of Photogrammetry and Remote Sensing*, *146*, 108-123, doi:10.1016/j.isprsjprs.2018.09.006.

Zhang, Y., and S. A. Klein (2010), Mechanisms Affecting the Transition from Shallow to Deep Convection over Land: Inferences from Observations of the Diurnal Cycle Collected at the ARM Southern Great Plains Site, *Journal of the Atmospheric Sciences*, *67*(9), 2943-2959, doi:10.1175/2010jas3366.1.

Accepted for publication in *Journal of the Atmospheric Sciences*. DOI 10.1175/JAS-D-21-0198.1.

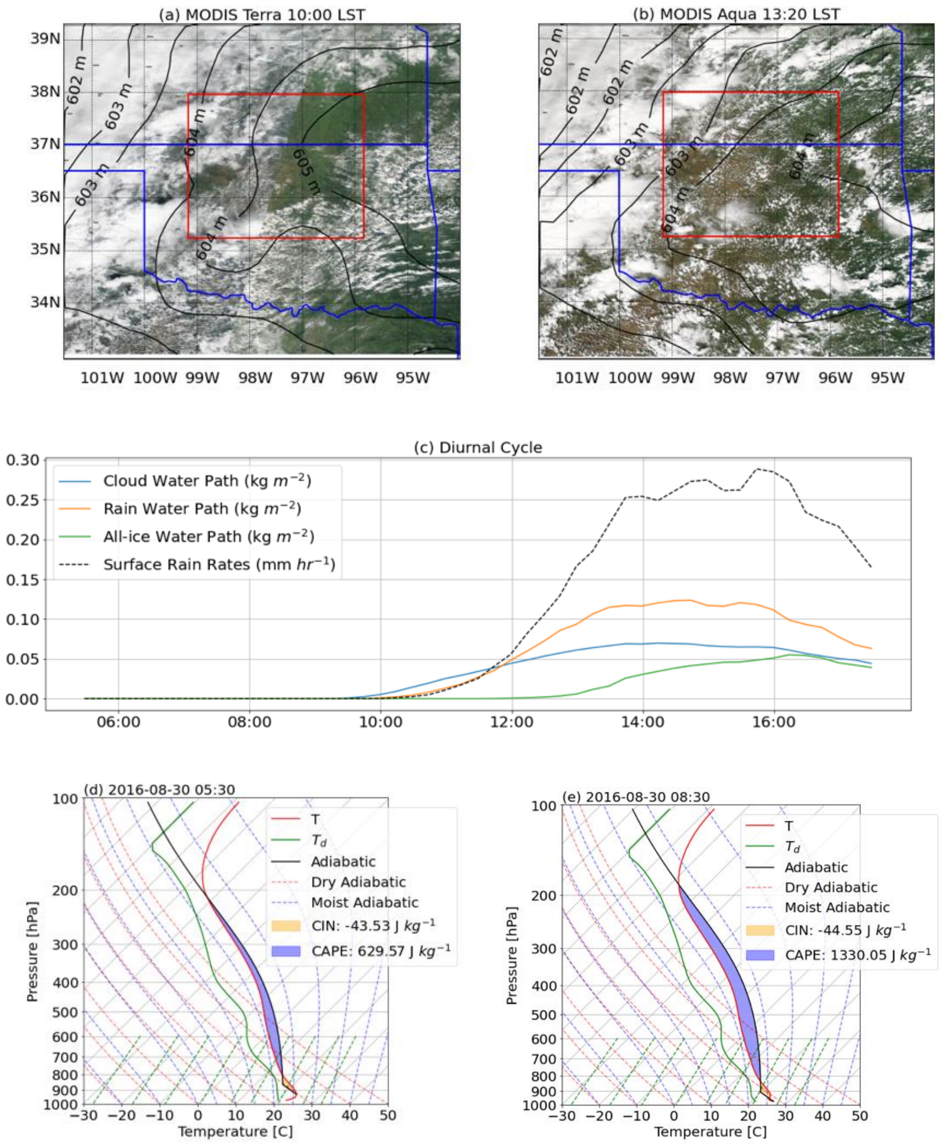

Figure 1. (a-b) Spatial distribution of clouds from MODIS with the red box as the simulation domain at 10:00 and 13:20 LST (16:30 and 19:50 UTC). The black contours are the geopotential height at 500 hPa at 16:00 and 20:00 UTC, respectively, based on ERA5 hourly data. Blue lines are the state boundaries. (c) diurnal cycle of hydrometeors and (d-e) domain mean of the vertical profile of initial and early morning temperature and moisture.

Accepted for publication in *Journal of the Atmospheric Sciences*. DOI 10.1175/JAS-D-21-0198.1.

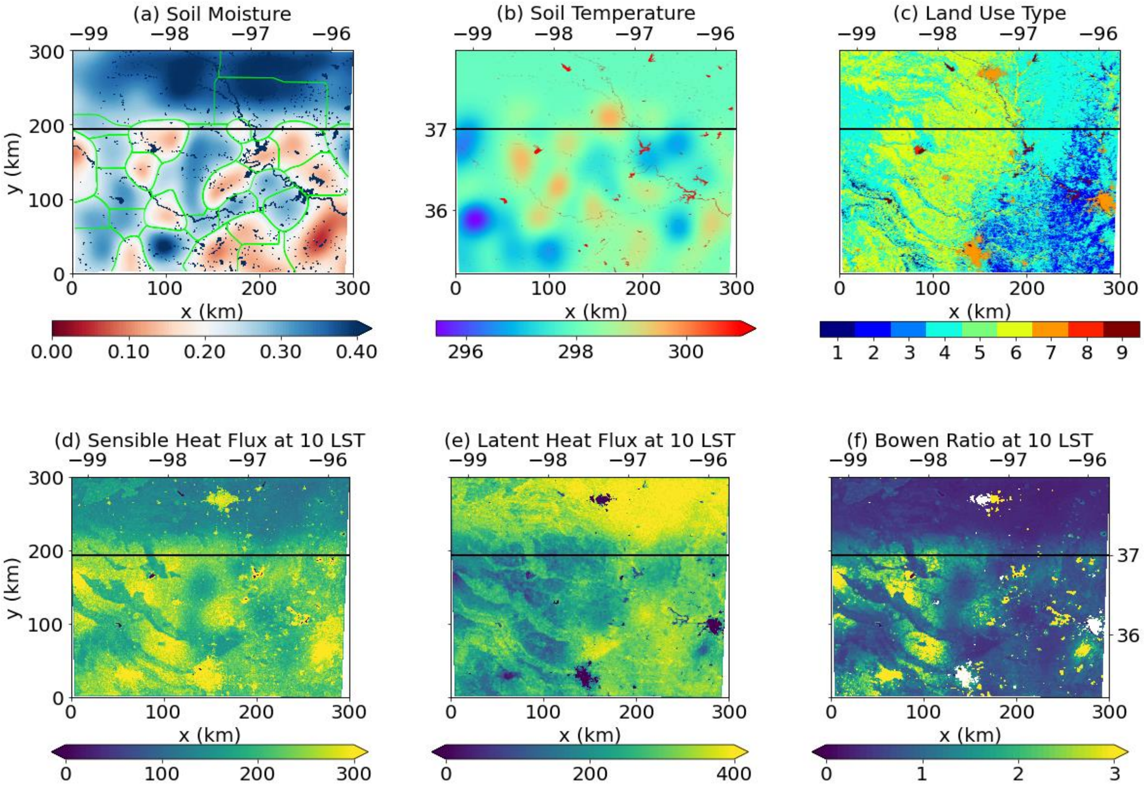

Figure 2. Spatial distribution of (a) initial soil moisture (unit: $m^3 m^{-3}$), (b) soil temperature, (c) land use type, (d) sensible heat flux at 10:00 LST (unit: W m^{-2}), (e) latent heat flux at 10:00 LST (unit: W m^{-2}), (f) Bowen ratio at 10:00 LST (unit: 1), Figures a-c are the same as Figure 1 in *Chen et al*. [2020]. In (a), green lines surround the soil moisture patches determined by the watershed. The land use types 1-9 are needleleaf forest, broadleaf forest, open shrublands, grasslands, permanent wetlands, croplands, urban and built-up, sparsely vegetated and water, respectively. The land use values were derived from a 30-m National Land Cover Database for 2011 [*Yang et al.*, 2018]. The horizontal black lines are the state boundary between Oklahoma and Kansas.

Accepted for publication in *Journal of the Atmospheric Sciences*. DOI 10.1175/JAS-D-21-0198.1.

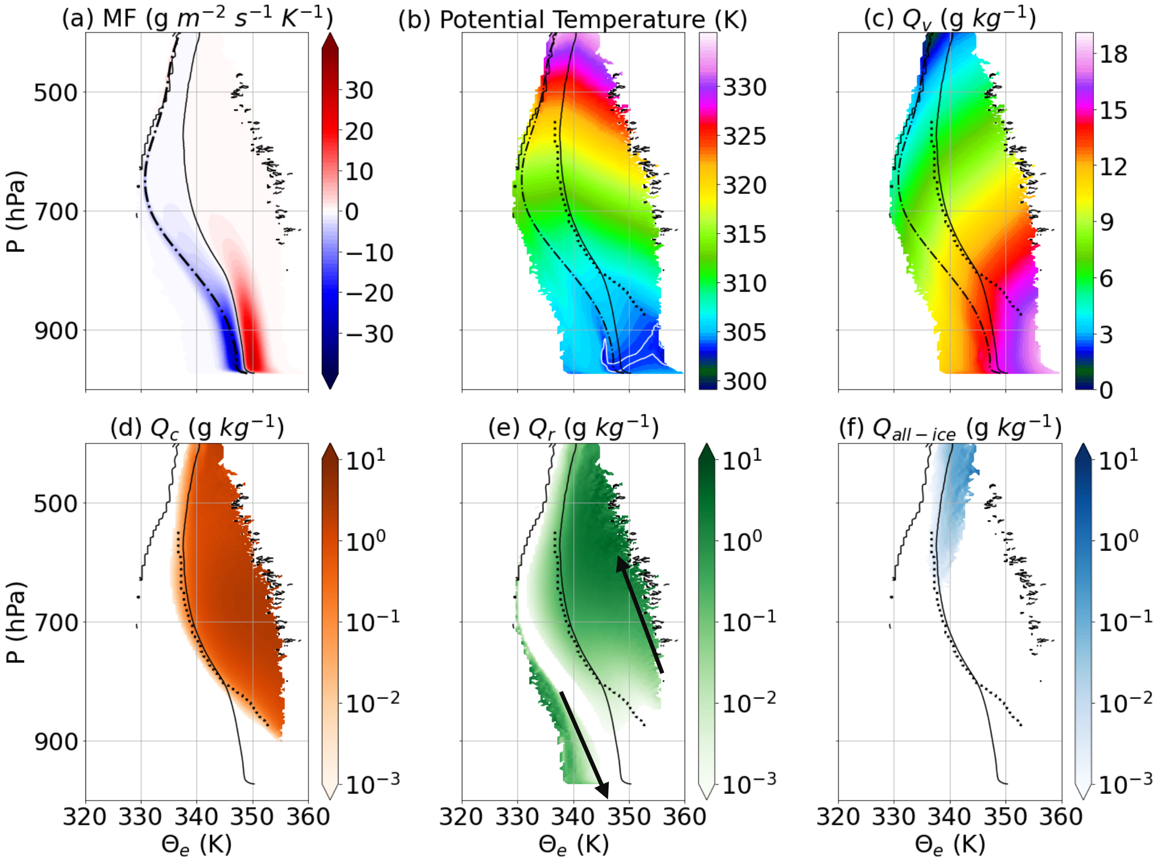

Figure 3. Isentropic analysis of (a) mass flux, (b) potential temperature, (c) water vapor mixing ratio, (d) cloud water mixing ratio, (e) rain water mixing ratio, and (f) all-ice water mixing ratio integrated from 6 to 12 LST. Solid black lines denotes where mass flux is zero. The dash-dot lines from Figures a-c are the domain-mean values of θ_e. Dotted lines represent the inflection line (See text for details). The white contour in Figure b marks the lowest 2% potential temperature.

Accepted for publication in *Journal of the Atmospheric Sciences*. DOI 10.1175/JAS-D-21-0198.1.

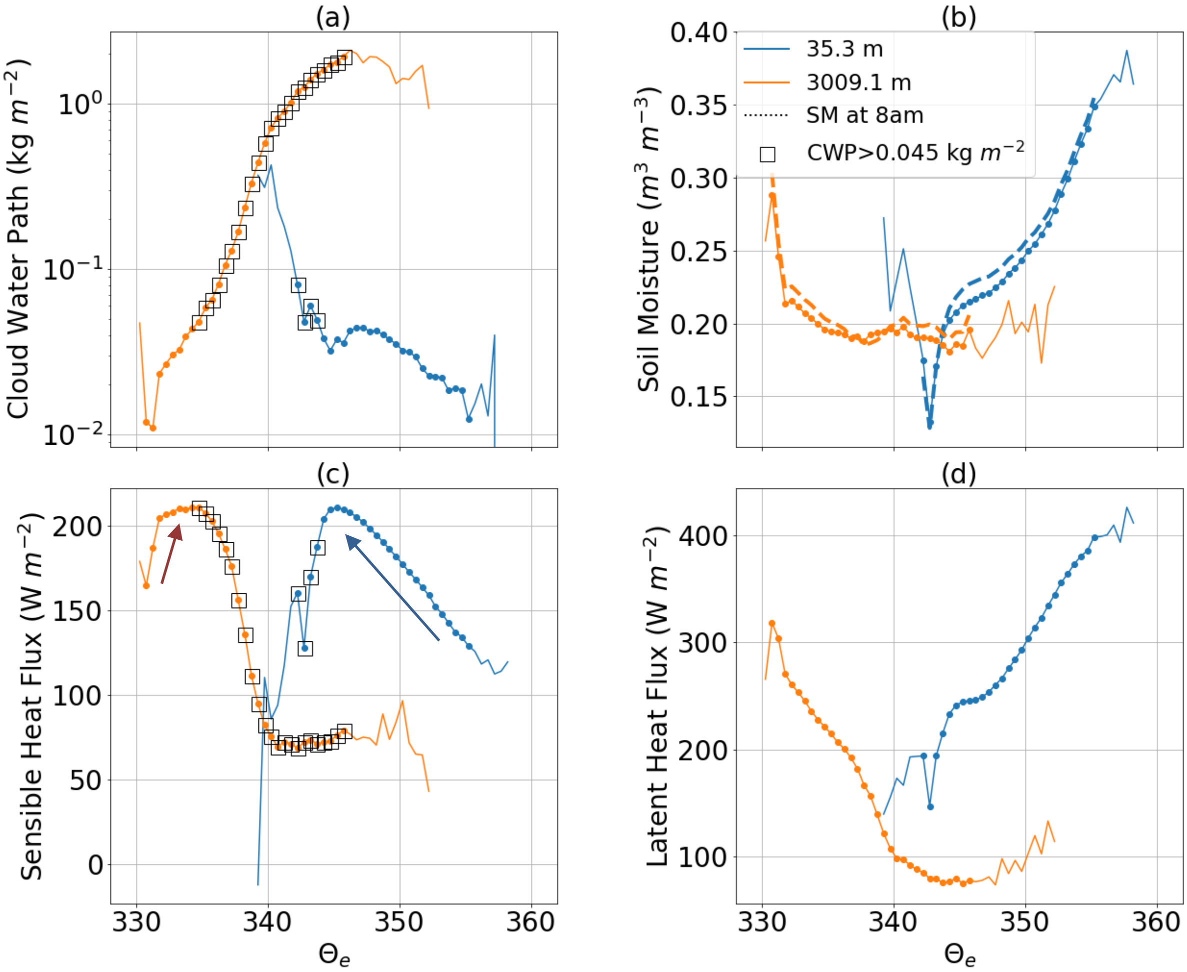

Figure 4. Isentropic analysis at 12:00 LST of (a) cloud water path, (b) soil moisture, (c) sensible heat flux, and (d) latent heat flux (lines and dots). Dash lines in Figure b refers to soil moisture at 8:00 LST without influences of precipitation. Square markers donate cloud water path larger than 0.045 kg m^{-2} when the cloud shading effect is prominent. Blue lines refer to the values close to the surface at 35.3m and orange lines refer to the values at the height where clouds exist at about 3009.1 m.

Accepted for publication in *Journal of the Atmospheric Sciences*. DOI 10.1175/JAS-D-21-0198.1.

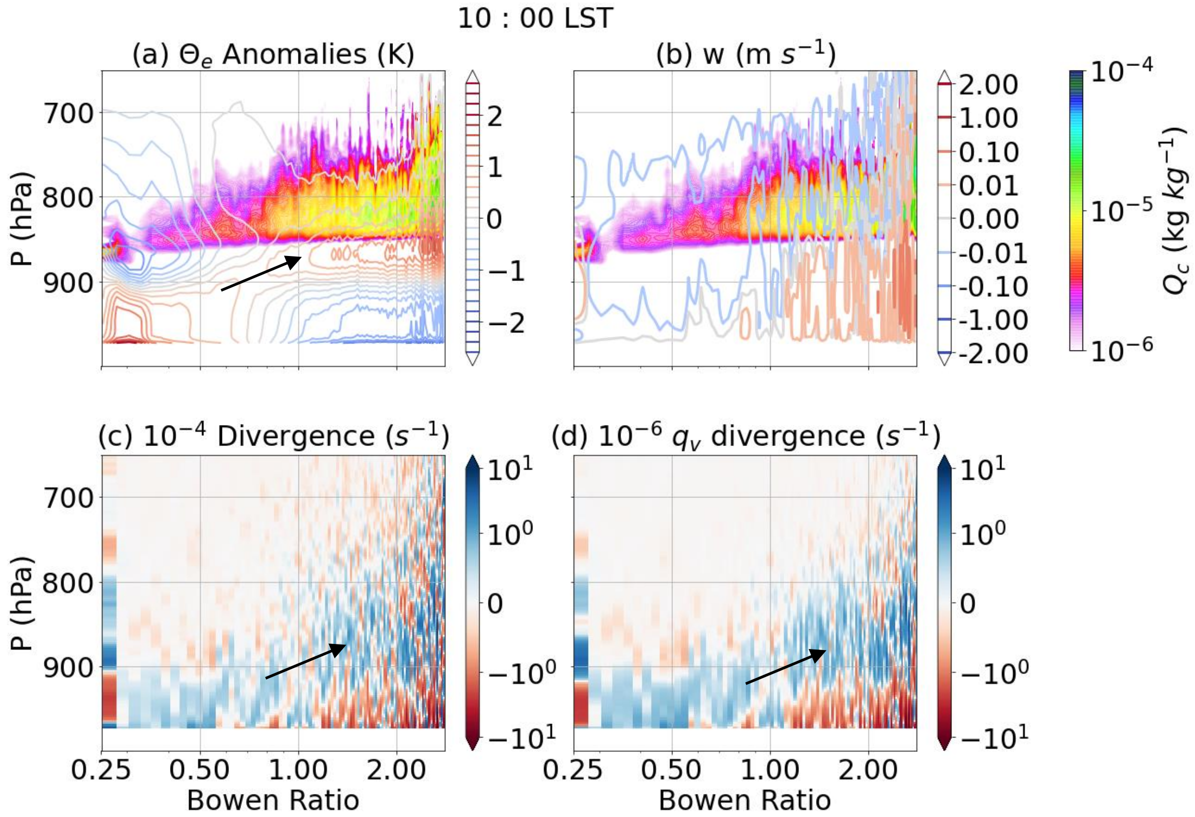

Figure 5. Averaged (a) θ_e anomalies, (b) vertical velocity, (c) air mass divergence, and (d) water vapor divergence at fixed Bowen ratio bins at 10:00 LST. Color shading represents cloud water mixing ratio. Plots are shown with a logarithmic x-axis.

Accepted for publication in *Journal of the Atmospheric Sciences*. DOI 10.1175/JAS-D-21-0198.1.

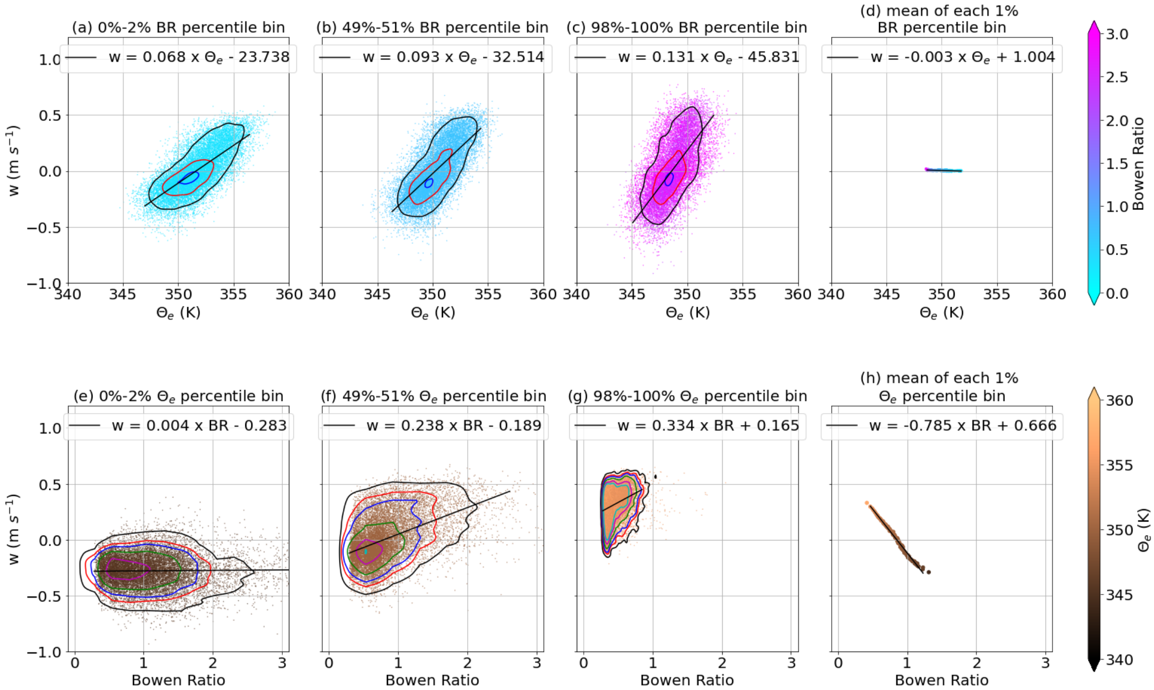

Figure 6. (a-c) Relationships between vertical velocity and θ_e with Bowen ratio at (a) 0-2%, (b) 49-51%, (c) 98-100% percentile bins at about 30m above the surface, and (d) mean vertical velocity and mean θ_e of each 1% Bowen ratio. (e-g) Relationships between vertical velocity and Bowen ratio with θ_e at (e) 0-2%, (f) 49-51%, (g) 98-100% percentile bins at ~30 m above ground level, and (h) mean vertical velocity and mean Bowen ratio of each 1% θ_e bin. Bowen ratios are the averaged values between 7:30 LST and 8:30 LST. Vertical velocity and θ_e are at 10:00 LST. Black, red, blue, green, magenta and cyan contours mark the kernel probability density function as 0.1, 0.3, 0.5, 1, 2 and 3.

Accepted for publication in *Journal of the Atmospheric Sciences*. DOI 10.1175/JAS-D-21-0198.1.

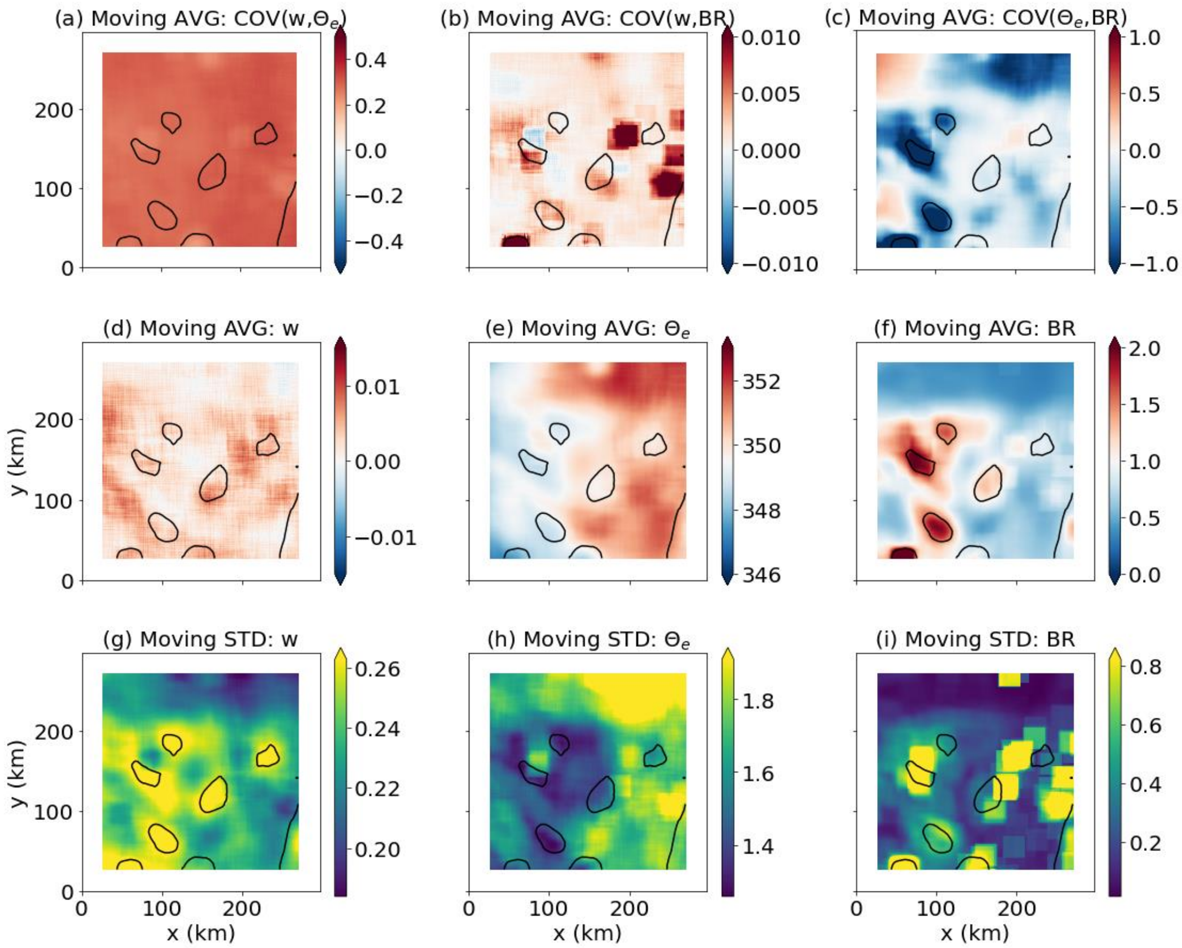

Figure 7. (a-c) moving averages of the covariance between w and θ_e, w and Bowen ratio, θ_e and bowen ratio, respectively. (d-f) Moving averages of w, θ_e and Bowen ratio (BR), respectively. (g-i) moving standard deviation of w, θ_e and Bowen ratio, respectively. The values of w and θ_e are at 10:00 LST and ~30 m above the surface. The side of moving box is 27 km in length. The black contours refer to surface sensible heat flux of 100 W m^{-2}. Bowen ratio and surface sensible fluxes are averaged between 7:30 and 8:30 LST.

Accepted for publication in *Journal of the Atmospheric Sciences*. DOI 10.1175/JAS-D-21-0198.1.

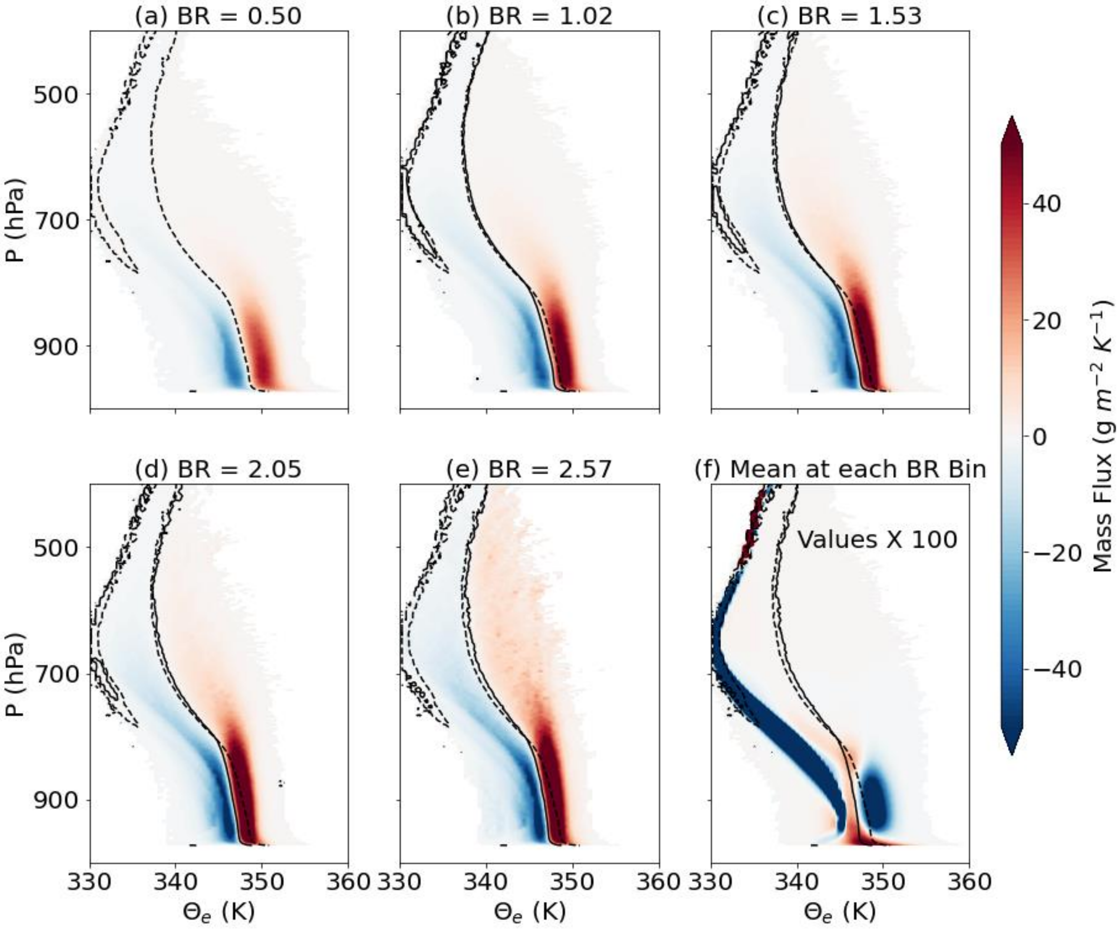

Figure 8. (a-e) Isentropic analysis of perturbed mass flux at five Bowen ratio bins with the median Bowen ratio values shown in the title. (f) Isentropic analysis of the averaged mass flux in each Bowen ratio bin. Dash lines show the zero mass flux when the median value of BR bin is 0.5. Solid lines in Figure b-f show the zero mass flux accordingly.

Accepted for publication in *Journal of the Atmospheric Sciences*. DOI 10.1175/JAS-D-21-0198.1.

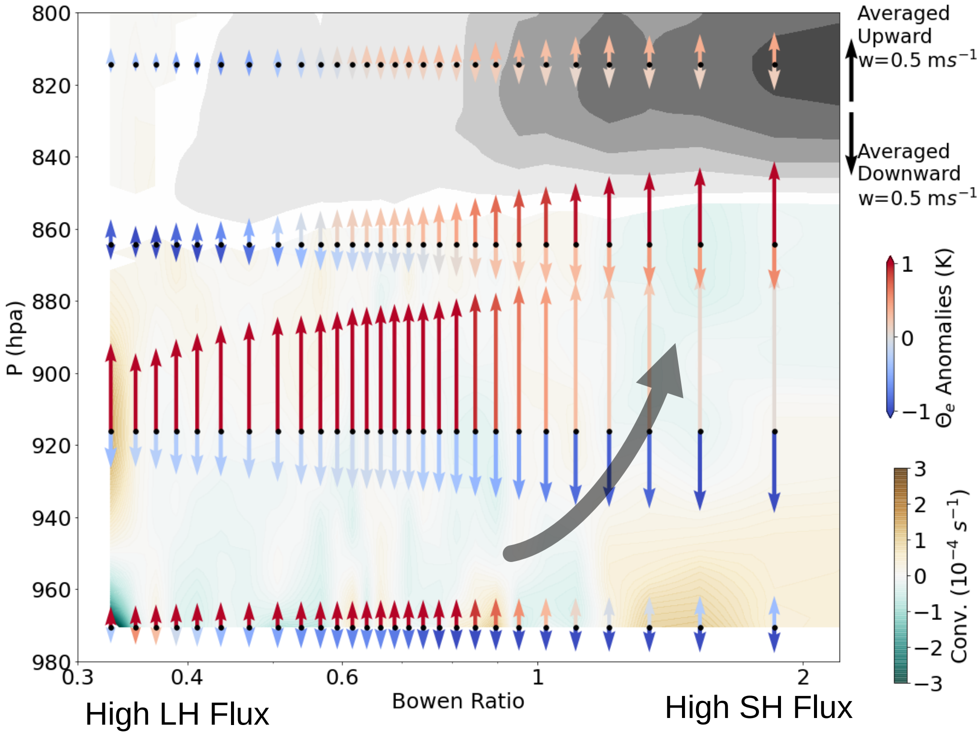

Figure 9. Summary diagram of energy transport associated with surface heterogeneity induced convective clouds by semi-idealized simulation. The grey shading denotes the cloud water mixing ratio, the color shading shows horizontal wind convergence, and the red and blue arrows are vertical motion conditionally averaged by their sign. The grey shaded arrow indicates that the mixing of the high θ_e parcel with high w parcel favors cloud formation.

Accepted for publication in *Journal of the Atmospheric Sciences*. DOI 10.1175/JAS-D-21-0198.1.

(a) (b)

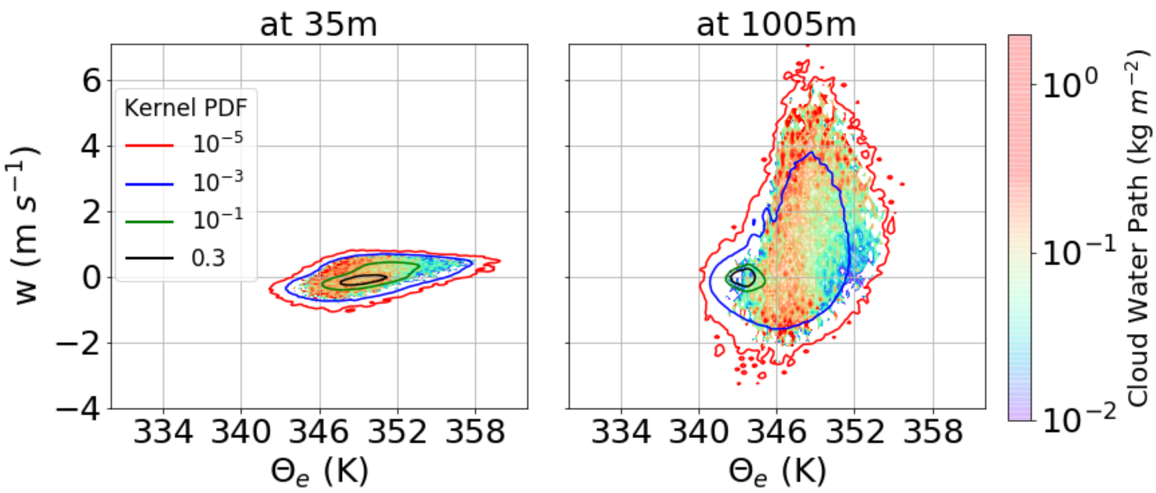

Figure 10. Gaussian Kernel PDF of vertical velocity (w) and equivalent potential temperature (θ_e) as contours. Shadings indicate averaged cloud water path at each w and θ_e bin. All the variables are at 10:00 LST.

Accepted for publication in *Journal of the Atmospheric Sciences*. DOI 10.1175/JAS-D-21-0198.1.

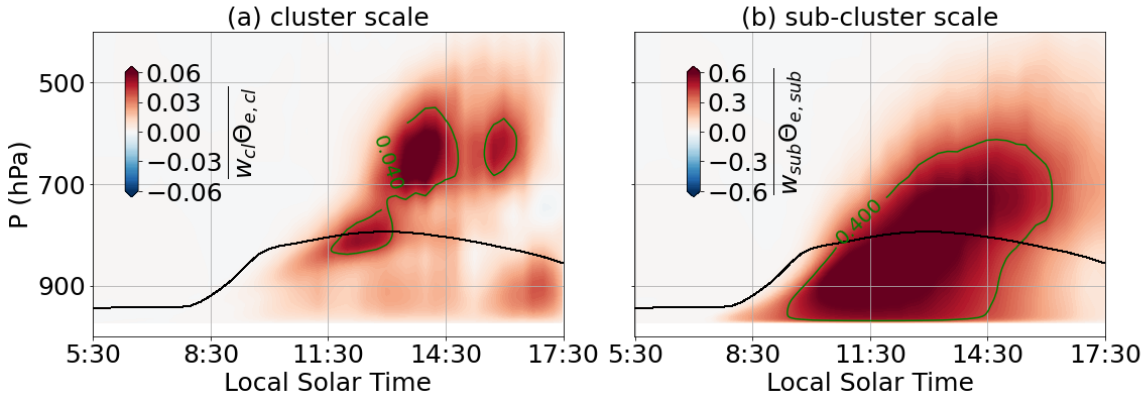

Figure 11. (a) Domain mean values of vertical transportation of entropy at the cluster scale. (b) Domain mean values of vertical transportation of entropy at the sub-cluster scale. Black lines are the boundary layer height.

Accepted for publication in *Journal of the Atmospheric Sciences*. DOI 10.1175/JAS-D-21-0198.1.

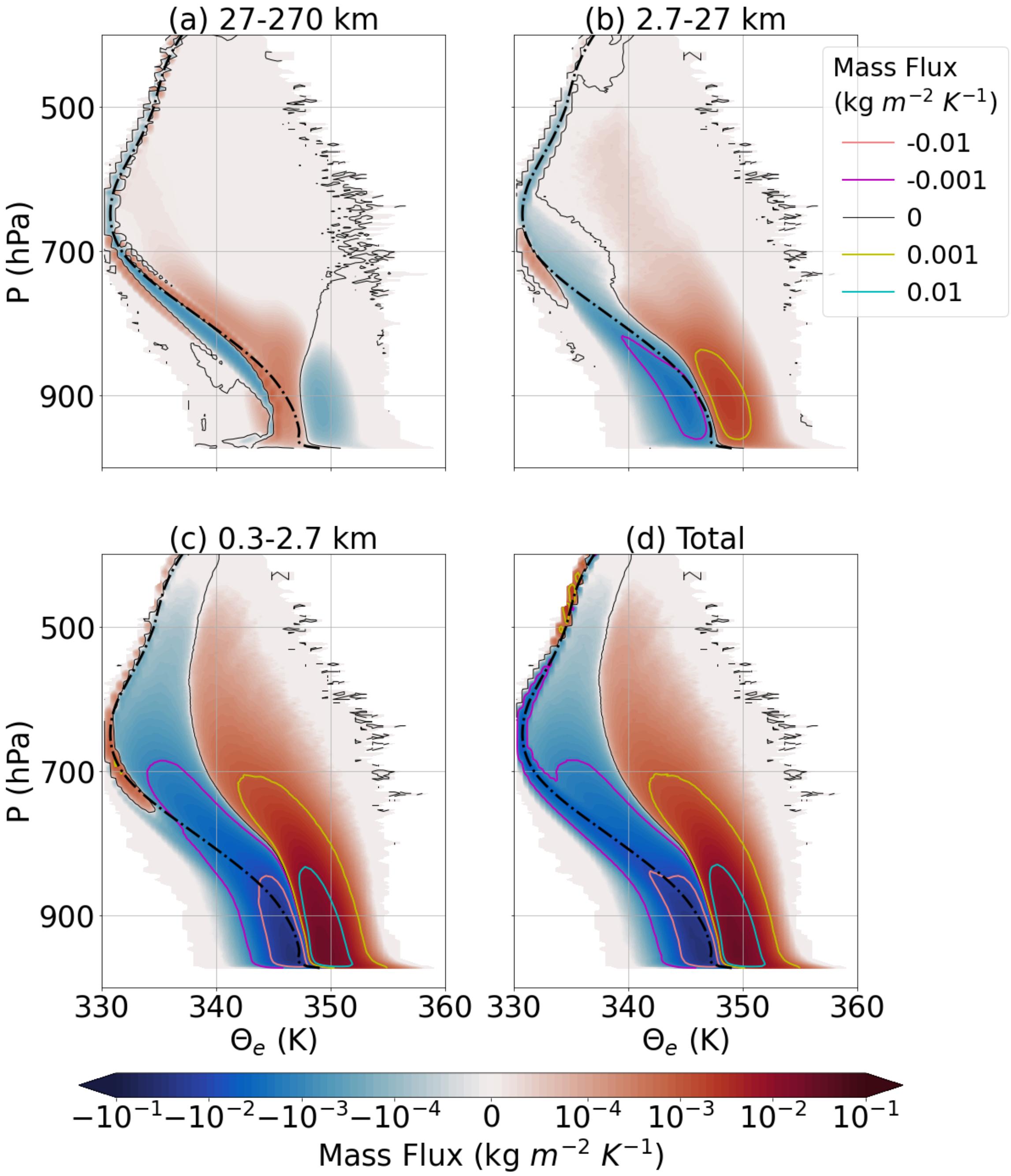

Figure 12. Isentropic mass flux at (a) 27-270 km, (b) 2.7-27 km, (c) 0.3-2.7 km and (d) all scale integrated from 6 to 12 LST. Dash-dot lines represent mean values of equivalent potential temperature.

Accepted for publication in *Journal of the Atmospheric Sciences*. DOI 10.1175/JAS-D-21-0198.1.

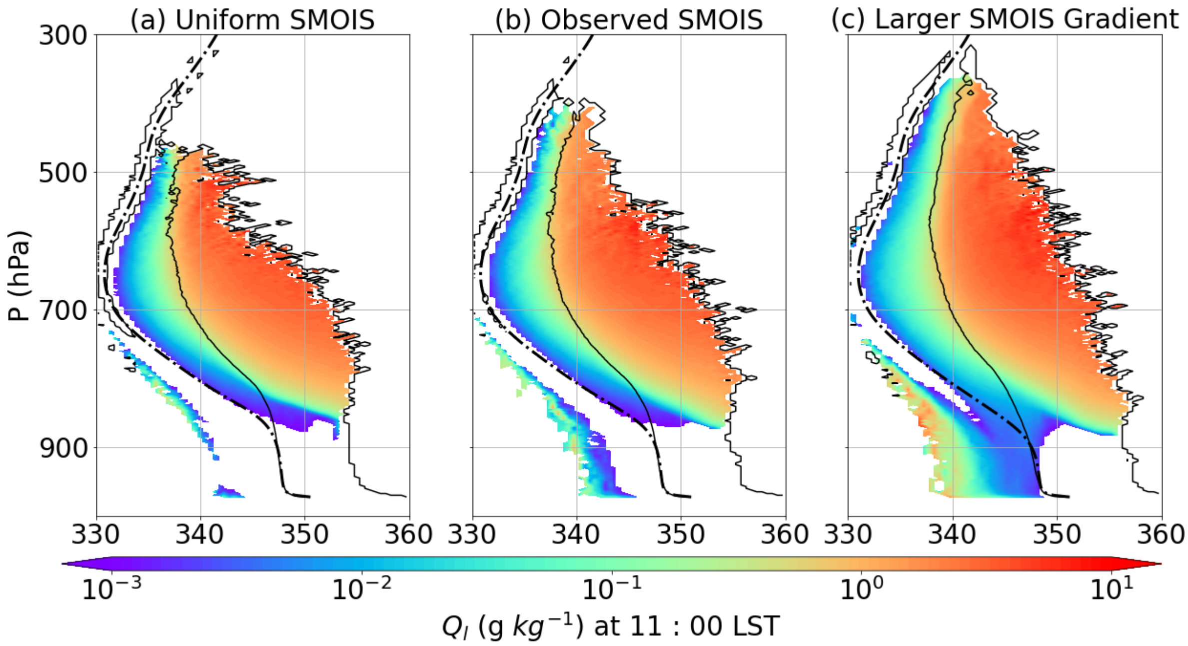

Figure 13. Isentropic analysis of liquid water mixing ratio at 11:00 LST with (a) uniform soil moisture, (b) observed soil moisture distribution, and (c) larger soil moisture gradient. Dash-dot lines represent the mean values of θ_e. Black lines donate the mass flux as zero.

Accepted for publication in *Journal of the Atmospheric Sciences*. DOI 10.1175/JAS-D-21-0198.1.

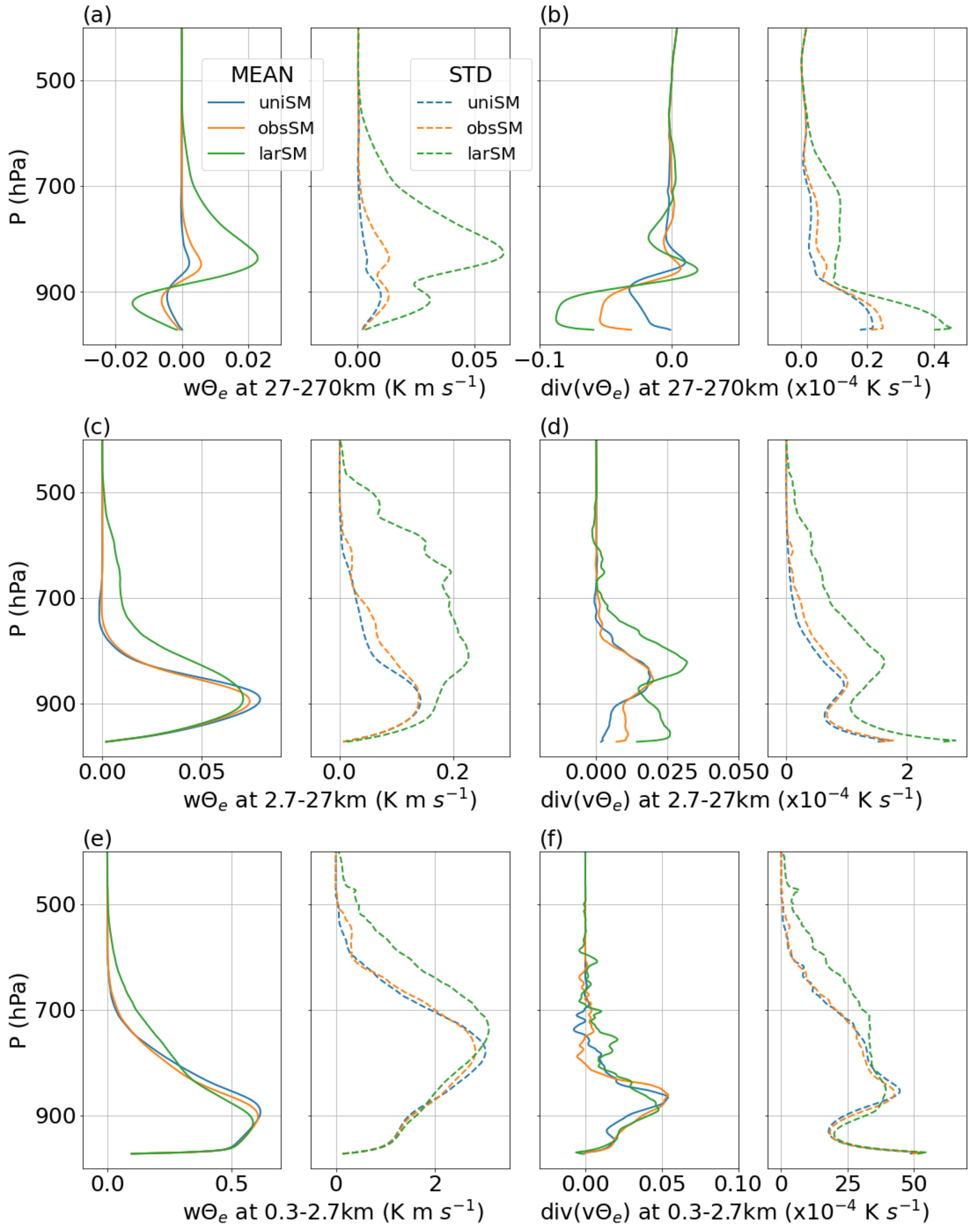

Figure 14. (a, c, and e) Vertical transport and (b, d, and f) horizontal divergence of θ_e at (a-b) 27-270 km, (c-d) 2.7-27 km and (e-f) 0.3-2.7 km at 10:30 LST.

Accepted for publication in *Journal of the Atmospheric Sciences*. DOI 10.1175/JAS-D-21-0198.1.

APPENDIX

Appendix Figures

(a) (b)

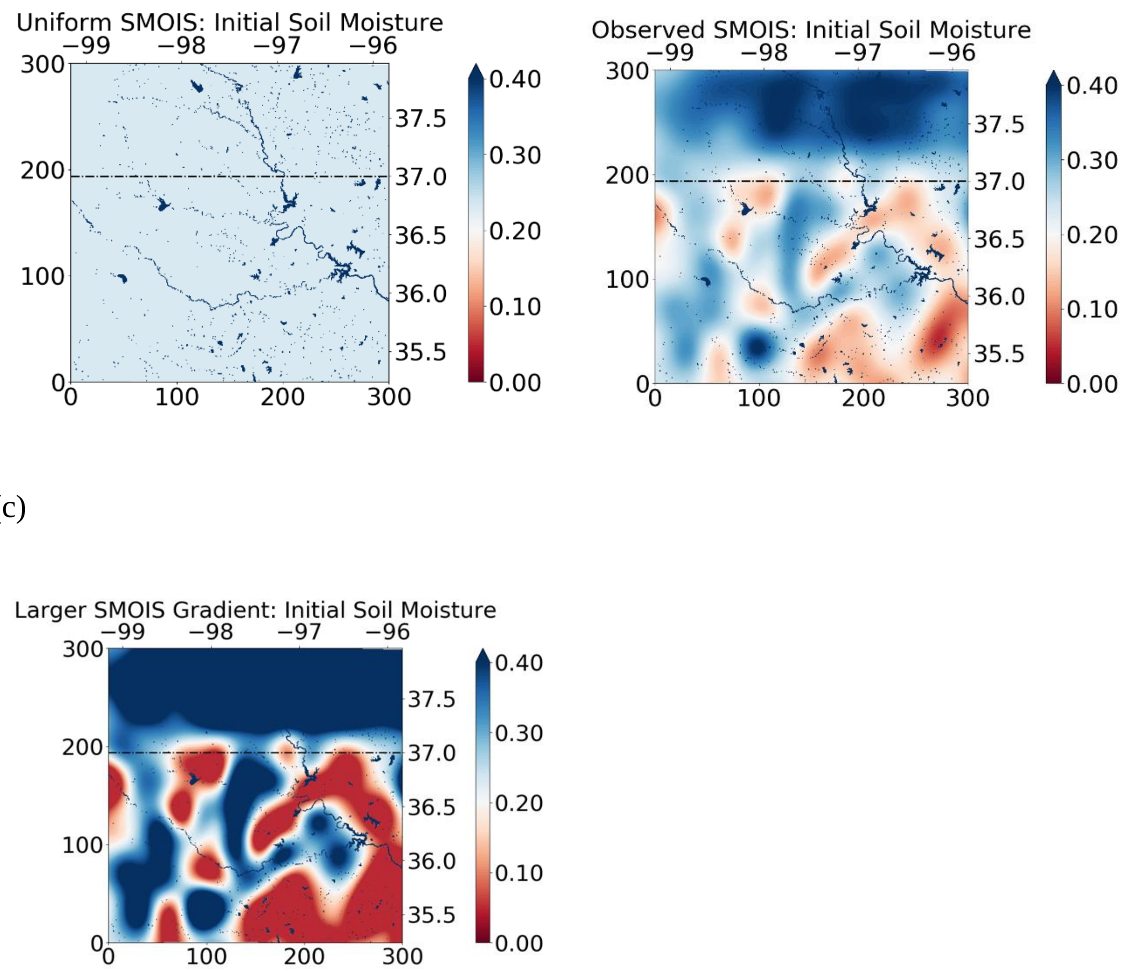

Figure A1. (a-c) Initial soil moisture of “uniSM”, “obsSM”, and “larSM” simulations.

Accepted for publication in *Journal of the Atmospheric Sciences*. DOI 10.1175/JAS-D-21-0198.1.